Probing leptophobic dark sectors via gravitational wave signatures

Taramati,[1,*] Lekhika Malhotra,[2,†] Zafri A. Borboruah,[2,‡] and Sudhanwa Patra[3,4,§]

[1]*Department of Physics, Indian Institute of Technology Bhilai, Durg-491002, India*
[2]*Indian Institute of Technology Bombay, Mumbai 400076, Maharashtra, India*
[3]*Department of Physics, Indian Institute of Technology Bombay, Mumbai 400076, India*
[4]*Institute of Physics, Bhubaneswar, Sachivalaya Marg, Bhubaneswar 751005, India*

(Received 2 January 2026; accepted 12 May 2026; published 6 July 2026)

We study a minimally extended version of the Standard Model where baryon number is gauged with a $U(1)_B$ symmetry. This model can be made anomaly-free by adding a set of additional fermions. The lightest component of these fermions behaves as a viable dark matter candidate. We show that the spontaneous breaking of $U(1)_B$ symmetry can produce gravitational waves via bubble dynamics resulting from a first-order phase transition, which can be detected in future gravitational wave experiments like LISA and ET. Such gravitational wave signatures can be used as a probe to constrain the model in future observations and complement dark matter and collider searches. We perform a random numerical scan of the parameter space and derive the viable region consistent with theoretical bounds from running of the coupling constants, current experimental bounds from dark matter experiments such as LUX-ZEPLIN and XENONnT and sensitive to future gravitational wave experiments. We find that dark matter with mass of 8–12 TeV is the most interesting to test in future gravitational wave as well as laboratory experiments. In the viable parameter space, the mass of the Z' gauge boson associated with the $U(1)_B$ lies in the 16–24 TeV range, and the mass of the scalar associated with the symmetry breaking lies around 1–2.5 TeV scale. Recent results from LUX-ZEPLIN rules out mass scales below TeV in this model, while dark matter with mass larger than 12 TeV will not be sensitive to future GW experiments. Hence, the dark matter and mediator mass scales of interest are marginally accessible at current collider energies.

DOI: 10.1103/rbnl-3zlf

I. INTRODUCTION

The Standard Model (SM) has been the most successful framework for understanding the building blocks of matter and their interactions, but it is far from the full story. It does not incorporate gravity in its description of particles [1], cannot explain the observed matter-antimatter asymmetry [2], offers no mechanism for neutrino masses and mixings [3–5], and does not account for the dark matter (DM) component of the Universe [6,7]. These limitations strongly suggest the existence of physics beyond the SM, leading to a rich landscape of theoretical models collectively known as beyond Standard Model (BSM) physics. One particularly intriguing idea is to minimally extend the SM gauge group by promoting the accidental global symmetries of the SM, like baryon number (B) or lepton number (L), to gauge symmetries, leading to new dynamics and new particles [8–22]. In these extended models, new gauge bosons and fermions emerge naturally, often paving the way for a viable dark matter candidate.

These BSM scenarios are difficult to test in laboratory experiments because they require very high energies. Gravitational waves (GWs) provide a complementary probe in this context. Since their first detection by LIGO in 2015 [23], GWs have become a valuable tool for studying the early Universe and searching for signatures of new physics. Recent results from the NANOGrav collaboration [24–30] confirms the presence of a stochastic gravitational wave background (SGWB) in the Universe. In particular, first-order phase transitions (FOPTs) associated with the spontaneous breaking of symmetries in BSM theories can generate SGWB that remain imprinted in spacetime [25,31–36]. These signals are largely unaffected by intervening matter or radiation, making them pristine messengers of high-scale dynamics [37–45]. In the context of dark matter, this connection is particularly compelling, since models that attempt to explain dark matter often introduce new symmetries, which may undergo FOPTs in the early

*Contact author: taramati@iitbhilai.ac.in
†Contact author: lekhika.malhotra@iitb.ac.in
‡Contact author: zafri123@iitb.ac.in
§Contact author: sudhanwa@iitbhilai.ac.in

Published by the American Physical Society under the terms of the Creative Commons Attribution 4.0 International license. Further distribution of this work must maintain attribution to the author(s) and the published article's title, journal citation, and DOI. Funded by SCOAP³.

Universe [46–59]. The resulting gravitational wave signatures serve not only as indirect evidence for the model but also as a means to constrain its parameter space. This makes gravitational wave astronomy a powerful tool that will complement dark matter searches and collider experiments.

Dark matter continues to evade detection despite extensive searches. In particular, weakly interacting massive particles (WIMPs) in the GeV to TeV mass range have been a central focus of interest. However, the lack of positive signals in direct detection experiments like LUX [60], XENON-100 [61], PANDAX-II [62,63] and XENON-1T [64,65], as well as in indirect detection probes like PAMELA [66,67], AMS-2 [68], Fermi-LAT [69] and IceCube [70,71], have imposed stringent limits on the parameter space of many WIMP-based models. These constraints have sparked a shift toward more sophisticated constructions where dark matter can evade detection while still accounting for the observed relic abundance [72–86]. It is now well established that purely singlet leptonic dark matter is largely excluded, as it tends to either overproduce relic density or yield spin-independent scattering cross sections in conflict with experimental limits [2,60,64,65,72,87]. A promising alternative lies in mixed dark matter states, particularly those arising from the mixing of SM singlets and doublets. Such constructions allow for significant suppression of couplings to the Z boson, thereby weakening direct detection signals without disrupting thermal freeze-out [88].

With the above motivation, in this paper, we aim to use future GW experiments to constrain the parameter space of a simple leptophobic extension of the SM, incorporating a fermionic dark matter candidate. Leptophobic models naturally forbid proton decay at the renormalizable level and allow new physics near the TeV scale without invoking a high-scale desert [17,18,20,21,89–94]. Such a framework not only ensures proton stability but also provides viable Majorana-type [18,89], Dirac-type [95,96], and vectorlike [97,98] dark matter candidates and uncovers novel avenues for baryogenesis. In this work, we extend the SM gauge group with a $U(1)_B$ local symmetry. To make the model anomaly-free, we add additional fermions to the particle content. Two of these extra fermions: one SM singlet and one doublet, mix through the scalar field that breaks the $U(1)_B$ symmetry [88]. The breaking of $U(1)_B$ symmetry not only gives masses to the dark sector but also leaves behind a Z_2 symmetry that stabilizes the dark matter candidate. Because this dark matter state is partially charged under the SM gauge group, it interacts with W and Z bosons, as well as the new Z' from the broken $U(1)_B$, offering interesting phenomenology for colliders and dark matter searches. If the symmetry breaking is first-order in nature, it proceeds via nucleation of bubbles. The dynamics of these bubbles, how they grow, collide, and stir up the surrounding plasma, produce a stochastic background of GWs. Future GW detectors like LISA [99], DECIGO/U-DECIGO [100,101], BBO [102,103], ET [104,105], etc., will reach sensitivities to probe phase transitions at the TeV scale and beyond. We demonstrate that a viable parameter space exists where the phase transition associated with $U(1)_B$ breaking is sufficiently strong to leave a distinct signature in the GW spectrum, peaked at frequencies that these instruments are designed to detect, making GWs an indirect probe of the dark sector.

This work is structured as follows: in Sec. II, we present the model framework, mass generation, and dark matter. Next in Sec. III, we evaluate the temperature-dependent effective potential for this model and define the phase transition properties and gravitational waves from the first-order phase transition. In Sec. IV, we present the current bounds on this model from electroweak precision experiments, dark matter direct and indirect detection experiments, and collider experiments. In Sec. V, we describe the methods we used for parameter scan of the model incorporating all the current bounds on the model while looking for a strong first-order phase transition with GW signatures detectable in future GW experiments. In this section, we show the results of the parameter scan and the complementarity of GW with laboratory experiments in probing this model. We conclude the paper in Sec. VI. Appendix A provides a brief description of the calculation of the relic density of the dark matter candidate. In Appendix B, we discuss the renormalization group evolution of the model parameters relevant for our numerical analysis.

II. MODEL

We consider a minimal $U(1)_B$ extension of the SM where baryon number is gauged. The SM particle content along with their $U(1)_B$ charges are given in Table I. Due to gauged baryon number, the nonzero anomalies that arise are [20,88],

$$\mathcal{A}[SU(2)_L^2 \otimes U(1)_B] = \frac{3}{2}, \qquad \mathcal{A}[U(1)_Y^2 \otimes U(1)_B] = -\frac{3}{2}. \tag{1}$$

TABLE I. Transformations of the SM particles.

SM Fermions	$SU(3)_C$	$SU(2)_L$	$U(1)_Y$	$U(1)_B$
$Q_L = \begin{pmatrix} u_L \\ d_L \end{pmatrix}$	**3**	**2**	1/6	1/3
u_R	**3**	**1**	2/3	1/3
d_R	**3**	**1**	−1/3	1/3
$\ell_L = \begin{pmatrix} \nu_L \\ e_L \end{pmatrix}$	**1**	**2**	−1/2	0
e_R	**1**	**1**	−1	0
Scalar				
H	**1**	**2**	1/2	0

TABLE II. Exotic fermions and scalars and their quantum charges.

Fermions	$SU(2)_L$	$U(1)_Y$	$U(1)_B$
$\Psi_L = \begin{pmatrix}\Psi_L^+ \\ \Psi_L^0\end{pmatrix}$	**2**	1/2	B_1
$\Psi_R = \begin{pmatrix}\Psi_R^+ \\ \Psi_R^0\end{pmatrix}$	**2**	1/2	B_2
ξ_L^+	**1**	1	B_2
ξ_R^+	**1**	1	B_1
χ_L	**1**	0	B_2
χ_R	**1**	0	B_1
Scalar			
S	**1**	0	$B_1 - B_2$

To cancel these anomalies, we add a pair of $SU(2)_L$ doublet fermions Ψ_L, Ψ_R and two pairs of singlet fermions χ_L, χ_R and ξ_L^+, ξ_R^+. To give these exotic fermions masses, we introduce a complex scalar singlet S that breaks the $U(1)_B$ symmetry. The quantum charges of these fields are presented in Table II. The nonzero anomalies are now given by,

$$\mathcal{A}[SU(2)_L^2 \otimes U(1)_B] = \frac{3}{2} + \frac{1}{2}(B_1 - B_2), \tag{2}$$

$$\mathcal{A}[U(1)_Y^2 \otimes U(1)_B] = -\frac{3}{2} - \frac{1}{2}(B_1 - B_2), \tag{3}$$

where B_1, B_2 are $U(1)_B$ quantum charges as shown in Table II. To ensure anomaly cancellation, the condition $B_1 - B_2 = -3$ must hold. Thus B_1 and B_2 can take various values [18,93]. In this paper, we choose $B_1 = -1$ and $B_2 = 2$, which provide us with a Dirac-type fermionic dark matter as we will discuss later.

A. Scalar sector

The scalar potential of our model can be written as [93,94,106],

$$V(H,S) = -\mu_H^2 H^\dagger H + \lambda_H (H^\dagger H)^2 - \mu_S^2 S^\dagger S + \lambda_S (S^\dagger S)^2 + \lambda_{HS}(S^\dagger S)(H^\dagger H), \tag{4}$$

where λ_{HS} is the portal coupling. The two scalars acquire vacuum expectation values (VEVs),

$$\langle S \rangle = \frac{v_B}{\sqrt{2}}, \qquad \langle H \rangle = \begin{pmatrix} 0 \\ v/\sqrt{2} \end{pmatrix}, \tag{5}$$

where $v = 246$ GeV and break the $U(1)_B$ and the electroweak symmetries. At the ground state, we can write the scalar fields as fluctuations around their respective VEVs as,

$$H = \frac{1}{\sqrt{2}} \begin{pmatrix} h^+ + iG^+ \\ v + \tilde{h} + iG_Z \end{pmatrix}, \qquad S = \frac{1}{\sqrt{2}}(v_B + \tilde{s} + iG_B), \tag{6}$$

where $\tilde{h}, \tilde{s}, G_Z, G_B$ are neutral while h^+, G^+ are charged real fields. Minimization of the potential with respect to the two VEVs eliminates the μ^2 terms, giving the mass matrix for the neutral scalars as,

$$M_{HS}^2 = \begin{pmatrix} 2\lambda_H v^2 & \lambda_{HS} v v_B \\ \lambda_{HS} v v_B & 2\lambda_S v_B^2 \end{pmatrix}. \tag{7}$$

This matrix has the eigenvalues,

$$m_h^2 = v^2\lambda_H + v_B^2\lambda_S - \sqrt{(v^2\lambda_H - v_B^2\lambda_S)^2 + (\lambda_{HS} v v_B)^2},$$
$$m_s^2 = v^2\lambda_H + v_B^2\lambda_S + \sqrt{(v^2\lambda_H - v_B^2\lambda_S)^2 + (\lambda_{HS} v v_B)^2}. \tag{8}$$

Here $m_h \simeq 125$ GeV is the mass of the SM Higgs particle. The scalar mixing angle θ is defined as,

$$\tan(2\theta) = \frac{\lambda_{HS} v v_B}{\lambda_H v^2 - \lambda_S v_B^2}. \tag{9}$$

The scalar masses can be written in terms of the mixing angle as,

$$m_h^2 = 2v^2\lambda_H \cos^2\theta + 2v_B^2\lambda_S \sin^2\theta + \lambda_{HS} v v_B \sin 2\theta,$$
$$m_s^2 = 2v^2\lambda_H \sin^2\theta + 2v_B^2\lambda_S \cos^2\theta - \lambda_{HS} v\, v_B \sin 2\theta. \tag{10}$$

The Goldstone modes have vanishing masses at zero temperature,

$$m_{h^+} = m_{G^+} = m_{G_Z} = m_{G_B} = 0. \tag{11}$$

However, as we shall see in the next section, at high temperatures, they have field-dependent nonzero masses which contribute to the 1-loop corrections to the tree-level potential. These Goldstone modes are *eaten up* by the gauge bosons of the theory to give masses to $W^\pm, Z$ bosons of the SM and the new Z' boson associated with the $U(1)_B$ symmetry [107,108].

The requirement for the potential to be bounded from below gives the following conditions [94],

$$\lambda_H > 0, \qquad \lambda_S > 0 \quad \text{and} \quad \sqrt{\lambda_H \lambda_S} + \frac{1}{2}\lambda_{HS} > 0. \tag{12}$$

Additionally, the perturbativity of the couplings imposes:

$$\lambda_H < 4\pi, \qquad \lambda_S < 4\pi \quad \text{and} \quad \lambda_{HS} < 4\pi. \tag{13}$$

B. Gauge sector

The masses of the neutral gauge bosons in our theory are as follows [108],

$$\begin{aligned} m_\gamma &= 0, \\ m_Z &= \frac{1}{2} v \sqrt{g^2 + g'^2} = 93 \pm 2 \text{ GeV}, \\ m_{Z'} &= 3 g_B v_B, \end{aligned} \tag{14}$$

where γ is the standard photon and g, g' are the gauge couplings associated with the $SU(2)_L$ and the $U(1)_Y$ gauge groups. Refer to [108] for the numerical values of the masses of charged gauge bosons $W^\pm$, which have their normal SM values.

C. Fermionic dark matter

After symmetry breaking, the exotic fermions in our model are odd under a remnant Z_2 symmetry while all the SM particles are even [80]. The four exotic fermions give rise to two neutral and two charged physical states. If the lightest of these four states is neutral, it can behave like a dark matter candidate stabilized by the Z_2 symmetry. The Yukawa Lagrangian for these fermions can be written as,

$$\begin{aligned} \mathcal{L}_Y = &-y_1 \overline{\Psi_L}\, \tilde{H}\, \xi_R^+ - y_2 \overline{\Psi_R}\, \tilde{H}\, \xi_L^+ - y_3 \overline{\Psi_L} H \chi_R - y_4 \overline{\Psi_R} H \chi_L \\ &- y_\psi \overline{\Psi_L} S \Psi_R - y_\xi \bar{\xi}_L^+ S^* \xi_R^+ - y_\chi \overline{\chi_L} S^* \chi_R, \end{aligned} \tag{15}$$

where $\tilde{H} = i\sigma_2 H^*$. The above Lagrangian can be reexpressed in terms of mass matrices as,

$$\begin{aligned} \mathcal{L}_Y = &\overline{\begin{pmatrix} \xi_L^+ & \Psi_L^+ \end{pmatrix}} \begin{pmatrix} M_\xi & M_2 \\ M_1 & M_\Psi \end{pmatrix} \begin{pmatrix} \xi_R^+ \\ \Psi_R^+ \end{pmatrix} \\ &+ \overline{\begin{pmatrix} \chi_L^0 & \Psi_L^0 \end{pmatrix}} \begin{pmatrix} M_\chi & M_4 \\ M_3 & M_\Psi \end{pmatrix} \begin{pmatrix} \chi_R^0 \\ \Psi_R^0 \end{pmatrix} + \text{H.c.}, \end{aligned} \tag{16}$$

where the different matrix elements are given as,

$$\begin{aligned} &M_1 = \frac{y_1 v}{\sqrt{2}}, \quad M_2 = \frac{y_2 v}{\sqrt{2}}, \quad M_3 = \frac{y_3 v}{\sqrt{2}}, \quad M_4 = \frac{y_4 v}{\sqrt{2}} \\ &M_\chi = \frac{y_\chi v_B}{\sqrt{2}}, \quad M_\Psi = \frac{y_\psi v_B}{\sqrt{2}}, \quad M_\xi = \frac{y_\xi v_B}{\sqrt{2}} \end{aligned} \tag{17}$$

For simplicity, we consider $M_3 = M_4$ and $M_1 = M_2$. In the small mixing limit, the neutral components of the singlet and doublet fermions combine to give rise to the physical states Ψ_1 and Ψ_2 with masses given by,

$$m_{\Psi_1} \simeq M_\chi + M_4 \sin 2\theta_{\text{DM}}, \qquad m_{\Psi_2} \simeq M_\Psi - M_4 \sin 2\theta_{\text{DM}}. \tag{18}$$

where θ_{DM} is the mixing angle defined by,

$$\tan 2\theta_{\text{DM}} = -\frac{2M_4}{M_\Psi - M_\chi}. \tag{19}$$

Similarly, the charged component of the doublet and the charged singlet mix to give rise to two physical states with mass eigenvalues,

$$m_{\Psi_1^+} \simeq M_\xi + M_2 \sin 2\theta_p, \qquad m_{\Psi_2^+} \simeq M_\Psi - M_2 \sin 2\theta_p, \tag{20}$$

with the mixing angle given by,

$$\tan 2\theta_p = -\frac{2M_2}{M_\Psi - M_\xi} \tag{21}$$

For $\sin\theta_{\text{DM}} = 0$, both χ and Ψ^0 (neutral component of Ψ) behave as independent dark matter candidates. For convenience, we only consider a single dark matter candidate in this paper, i.e., $\sin\theta_{\text{DM}} > 0$. Smaller $\sin\theta_{\text{DM}}$ signifies that the DM is mainly of singlet type, while a larger $\sin\theta_{\text{DM}}$ implies that the primary contribution to the DM is from the doublet. We take $\sin\theta_p$ to be negligibly small for simplicity. Additionally, we consider $y_\xi \gg y_\psi \gg y_\chi$ such that Ψ_1 is always the DM candidate and the charged fermions can decay to DM. In addition, Ψ_1^+ is now the heaviest, required for collider phenomenology to be discussed in the next section. In the small $\sin\theta_{\text{DM}}$ and $\sin\theta_p = 0$ limit, $m_{\Psi_2^+} \simeq m_{\Psi_2}$.

III. PHASE TRANSITION

In this section, we explore the parameter space of our model that gives rise to a strong first-order phase transition. Such phase transitions are associated with the nucleation of bubbles of true vacua that expand approximately at the speed of light and collide with each other, producing gravitational waves in the process. We study the GW signals that can be detected in future GW experiments such as LISA, BBO and ET, complementing DM and collider searches.

A. The effective potential

The dynamics of the fields and the spontaneous breaking of $U(1)_B$ depend on the temperature-dependent effective potential, V_{eff} of the theory. From a phenomenological perspective, we are interested in the scenario where the $U(1)_B$ breaking scale is much higher than the electroweak breaking scale, $v_B \gg v$. In this limit, the tree-level potential can be written from Eq. (4),

$$V_0(\varphi_S) = -\frac{\mu_S^2}{2}\varphi_S^2 + \frac{\lambda_S}{4}\varphi_S^4 \tag{22}$$

where $\varphi_S = v_B + \tilde{s}$ is the real part of the complex field S given in Eq. (6). The effective potential can be written as [44,50,109]

$$V_{\rm eff}(\varphi_S,T) = V_0(\varphi_S) + V_{\rm CW}(\varphi_S) + V_{\rm CT}(\varphi_S) + V_{\rm T}(\varphi_S,T) + V_D(\varphi_S,T) \tag{23}$$

The different potential terms are explained below: $V_{\rm CW}(\varphi_S)$ is the 1-loop Coleman-Weinberg (CW) contribution, renormalized in the $\overline{\rm MS}$ scheme in the Landau gauge, given by [50,110]

$$V_{\rm CW}(\varphi_S) = \frac{1}{64\pi^2}\sum_i n_i(-1)^{2s_i} m_i^4(\varphi_S) \times \left(\log\left[\frac{m_i^2(\varphi_S)}{\Lambda^2}\right] - C_i\right). \tag{24}$$

Here, $m_i(\varphi_S)$ are the field-dependent masses of all the bosonic and fermionic states (including Goldstones) in our model and the summation runs over i, denoting these states. The relevant gauge and fermion sector masses are given by Eqs. (14), (18), and (20) by replacing v_B with φ_S and taking $v \approx 0$ while the scalar masses are given by,

$$m_h^2 = -\mu_H^2 + \frac{\lambda_{HS}\varphi_S^2}{2}, \qquad m_s^2 = -\mu_S^2 + 3\lambda_S\varphi_S^2 \tag{25}$$

where μ_H^2, μ_S^2 are obtained by minimizing the tree-level potential with respect to the VEVs v and v_B. The Goldstone bosons acquire masses,

$$m_{h^+,G^+,G_Z}^2 = -\mu_H^2 + \frac{\lambda_{HS}\varphi_S^2}{2}, \qquad m_{G_B}^2 = -\mu_S^2 + \lambda_S\varphi_S^2 \tag{26}$$

In this calculation, Λ represents the renormalization scale, which we set to be v_B. Although we are working in the Landau gauge, the mass eigenvalues of the Goldstones can be nonzero even for $T = 0$, as these are evaluated at field configurations rather than the tree-level VEVs at zero temperature. The spin and the number of degrees of freedom (dof) of a particle i is denoted by s_i and n_i, respectively, e.g. $s_i = 1$ for bosons and $1/2$ for fermions while $n_i = 1$ for scalar states h, s, h^+, G^+, G_Z, G_B, $n_i = 3$ for Z', one of which is the longitudinal mode, $n_i = 4$ for the Dirac fermions $\Psi_1, \Psi_2, \Psi_1^+, \Psi_2^+$. Moreover, in the $\overline{\rm MS}$ scheme: $C_i = 3/2$ for scalars and fermions and $5/6$ for vector bosons. Note that in the assumed limit $v \ll v_B$, our phase transition analysis and hence the GW spectrum is not sensitive to the mixing angles $\sin\theta_{\rm DM}$ and $\sin\theta_p$ from the previous section.

When we check the masses and mixings resulting from the effective potential, they deviate from their predicted tree-level values even at zero temperature. So we impose an appropriate counterterm to renormalize the potential to preserve the tree-level values of the mixing and masses [44,50,111,112],

$$V_{\rm CT}(\varphi_S) = -\frac{\delta\mu_S^2}{2}\varphi_S^2 + \frac{\delta\lambda_S}{4}\varphi_S^4 \tag{27}$$

where the coefficients of the counterterms can be calculated by minimizing the zero-temperature effective potential with the counterterms and demanding,

$$\left.\frac{\partial V_{\rm CT}(\varphi_S)}{\partial\varphi_S}\right|_{\varphi_S=v_B} = -\left.\frac{\partial V_{\rm CW}(\varphi_S)}{\partial\varphi_S}\right|_{\varphi_S=v_B} \tag{28}$$

$$\left.\frac{\partial^2 V_{\rm CT}(\varphi_S)}{\partial\varphi_S^2}\right|_{\varphi_S=v_B} = -\left.\frac{\partial^2 V_{\rm CW}(\varphi_S)}{\partial\varphi_S^2}\right|_{\varphi_S=v_B} \tag{29}$$

Our choice of the renormalization condition makes sure that the zero-temperature VEV of the effective potential is the same as the VEV of the tree-level potential. Next we write the finite temperature one-loop quantum correction term [44,50,112–114],

$$V_{\rm T}(\varphi_S,T) = \frac{T^4}{2\pi^2}\sum_i n_i J_i\left(\frac{m_i^2(\varphi_S)}{T^2}\right), \tag{30}$$

where the summation is again taken over all scalars, fermions, and vector bosons (both transverse and longitudinal components). The thermal functions are defined by the following integrals [112,113,115–117],

$$J_{B,F}(y^2) = \int_0^\infty {\rm d}x\, x^2 \log\left(1 \mp e^{-\sqrt{x^2+y^2}}\right). \tag{31}$$

Here $\mp$ sign denotes bosons and fermions, respectively. At high temperatures, finite-temperature perturbation theory breaks down due to infrared divergences for bosonic modes [118] in the finite temperature potential when $T \gg m$. "Daisy resummation" is the typical method used to resum these states [119]. Here, we employ the Espinosa technique [116], which gives the contribution,

$$V_D(\varphi_S) = -\frac{T}{12\pi}\sum_i n_i\left[(m_i^2(\varphi_S) + \Pi_i(T))^{3/2} - (m_i^2(\varphi_S))^{3/2}\right], \tag{32}$$

where i now only runs over the scalar fields and the longitudinal component of the dark photon. The one-loop thermal masses $\Pi_a(T)$ in our model are given by,

$$\Pi_{\tilde{s}}(T) = \left(\frac{\lambda}{3} + \frac{(y_\chi + y_\xi + y_\psi)^2}{12} + \frac{g^2}{4}\right)T^2 \tag{33}$$

$$\Pi_{G_B}(T) = \left(\frac{\lambda}{3} + \frac{(y_\chi + y_\xi + y_\psi)^2}{12} + \frac{g^2}{4}\right)T^2 \tag{34}$$

$$\Pi_{Z'}(T) = \left(\frac{1}{12} + \frac{2}{3}\right)g^2T^2. \tag{35}$$

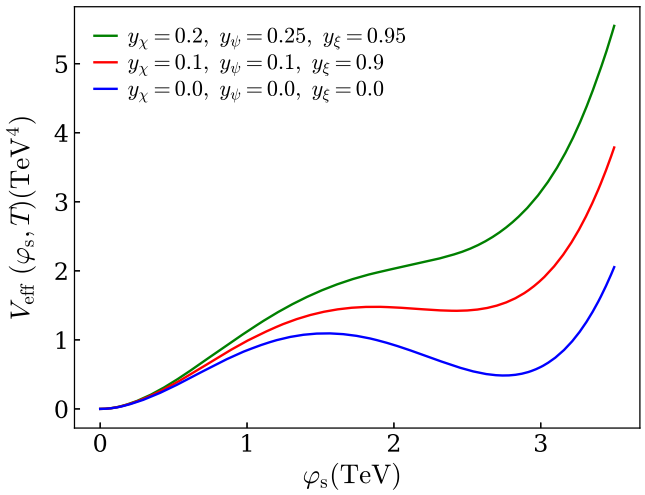


FIG. 1. Plot of $V_{\rm eff}(\varphi_S, T)$ given in Eq. (23) a temperature $T = 2.27$ TeV, with quartic coupling $\lambda_S = 10^{-3}$, $v_B = 5$ TeV and $g_B = 0.67$. Different colored lines represent different values of the Yukawa couplings y_χ, y_ψ, y_ξ.

In order to avoid using the thermal mass of the DM fermion in our calculations, we only resum the Matsubara zero modes in the daisy potential, which are the ones creating the infrared divergences of Eq. (32).

In Fig. 1, we show $V_{\rm eff}$ as a function of the field φ_S at temperature $T = 2.27$ TeV for a sample parameter point $\lambda_S = 0.0035$ and $g_B = 0.67$ while varying the Yukawa couplings $y_{\chi,\psi,\xi}$. The presence of exotic fermions tends to destabilize the Higgs vacua at v_B for nonzero values of the Yukawa couplings due to their negative contribution in the Coleman-Weinberg corrections. To make sure that the effective potential is bounded from below, we check the condition that at zero temperature, $\varphi_S = v_B$ is the global minimum of the effective potential for each parameter choice we make, i.e. for large field values, $V_{\rm eff}(\varphi_S, 0) > V_{\rm eff}(v_B, 0)$.

B. Phase transition properties

The $U(1)_B$ symmetry is spontaneously broken at low temperatures at the global minima of the effective potential. This phase transition can be of first or second order, depending on the parameter values. First-order phase transition occurs through the nucleation of bubbles of the broken phase in the unbroken Universe. At higher temperatures, $V_{\rm eff} \propto T^2\varphi_S^2$; hence, the global minimum is at $\varphi_S = 0$. As the temperature drops, another local minimum develops at $\varphi_S = v_B(T)$. At a critical temperature T_c, the two minima become degenerate. We are interested in identifying the subset of the parameter space for which there is a potential barrier between the two degenerate minima at T_c, which is necessary for a first-order phase transition. Below T_c, the temperature-dependent nonzero minima become the global minima while the Universe remains in the symmetric phase, which is now a metastable state. There is a finite probability that the field s would tunnel to the global minima, bringing the Universe to the symmetry broken phase. The tunneling rate is given by [44,120,121],

$$\Gamma(T) \approx T^4 \left(\frac{S_3}{2\pi T}\right)^{3/2} e^{-\frac{S_3}{T}}, \tag{36}$$

where S_3 is the three-dimensional Euclidean action evaluated for the critical bubble corresponding to the bounce solution [110]. The bubble profile $s(x, T)$ can be calculated by solving the equation of motion,

$$\frac{d^2\varphi_S}{dx^2} + \frac{2}{x}\frac{d\varphi_S}{dx} = \frac{dV_{\rm eff}(\varphi_S, T)}{d\varphi_S} \tag{37}$$

with boundary conditions $d\varphi_S/dx = 0$ at $x = 0$ and $\varphi_S \to 0$ as $x \to \infty$ where x is the 3D radial coordinate. S_3 is then defined as,

$$S_3 = \int_0^\infty \mathrm{d}x\mathrm{d}x^2 \left[\frac{1}{2}\left(\frac{\mathrm{d}\varphi_S(x)}{\mathrm{d}x}\right)^2 + V(\varphi_S, T)\right]. \tag{38}$$

The transition is typically identified by the nucleation temperature $T_n < T_c$, which is the temperature at which the nucleation really takes place. It is defined as the temperature at which there is at least one nucleation per Hubble horizon,

$$\int_{T_n}^{T_c} \frac{\mathrm{d}T}{T}\frac{\Gamma(T)}{\mathcal{H}(T)^4} = 1. \tag{39}$$

where $\mathcal{H}(T)$ is the Hubble parameter given as,

$$\mathcal{H}(T)^2 = \frac{\rho_{\rm rad}(T) + \rho_{\rm vac}(T)}{3M_{\rm pl}^2} = \frac{1}{3M_{\rm pl}^2}\left(\frac{\pi^2}{30}g_* T^4 + \Delta V(T)\right) \tag{40}$$

with g_* is the relativistic degrees of freedom at temperature T for our model and $M_{\rm pl} = 2.435 \times 10^{18}$ GeV, the reduced Planck mass. The vacuum energy density is calculated from $\Delta V(T) = V_{\rm eff}(0, T) - V_{\rm eff}(v_B(T), T)$. In radiation-dominated epoch, the condition for nucleation temperature in Eq. (39) can be approximated by [122],

$$\frac{S_3}{T_n} \sim -4\log\frac{1.66\sqrt{g_*}T_n}{M_{\rm pl}} \sim 100 - 140 \tag{41}$$

for $T_n \sim 10^6 - 10^2$ GeV. The nucleated bubbles are spherically symmetric and after nucleation, they expand and collide while interacting with the surrounding plasma. These collisions and plasma interactions are the sources of gravitational waves from FOPT. If the phase transition is

of second order or not strongly first order, there is no tunneling, hence no bubble formation. In that case, the field smoothly rolls down to the true vacuum at lower temperatures and no GWs are emitted.

In the case of FOPT, tunneling does not imply that the whole Universe will transform into the symmetry-broken phase. Therefore, we need another temperature to characterize the phase transition, called the percolation temperature $T_p \lesssim T_n$, at which a significant portion of the Universe (approximately 70%) is converted into the broken phase via merging of expanding bubbles. We calculate it by defining the probability of a point in space still being in the false vacuum at temperature T to be $P(T) = e^{-I(T)}$, where $I(T)$ is the volume of true vacuum per unit comoving volume [123],

$$I(T) = \frac{4\pi}{3}\int_T^{T_c} dT' \frac{\Gamma(T')}{T'^4 \mathcal{H}(T')}\left(\int_T^{T'} \frac{d\tilde{T}}{\mathcal{H}(\tilde{T})}\right)^3 \quad (42)$$

From 3D percolation theory, the percolation temperature is calculated using the condition $I(T_p) = 0.34$ [124]. We find that $T_p \sim T_n$ for all the parameter points considered in our random scan, hence we calculate all the GW parameters at T_n.

To obtain the GW spectrum, we need to calculate two parameters, α and β. The parameter α measures the strength of the phase transition and corresponds to the vacuum energy released during the phase transition, normalized by the total radiation energy density [125],

$$\alpha = \frac{\rho_{\rm vac}}{\rho_{\rm rad}} = \frac{1}{\rho_{\rm rad}}\left[\frac{T}{4}\frac{\mathrm{d}\Delta V}{\mathrm{d}T} - \Delta V\right]_{T_n} \quad (43)$$

Here, radiation energy density $\rho_{\rm rad}$ is given by $\rho_{\rm rad} = \frac{g_\star \pi^2 T^4}{30}$. The parameter β signifies the inverse time duration of the phase transition [126], namely,

$$\beta = \left(\mathcal{H} T \frac{\mathrm{d}(S_3/T)}{\mathrm{d}T}\right)_{T_n} \quad (44)$$

In our analysis, the effective potential is computed in the Landau gauge, which is a standard choice in studies of finite-temperature phase transitions as it simplifies the treatment of Goldstone modes and thermal corrections. We note, however, that the perturbative effective potential and quantities derived from it, such as the critical temperature T_c, nucleation temperature T_n, and the phase transition parameters $(\alpha, \beta/\mathcal{H})$, are in general gauge dependent. This issue has been extensively discussed in the literature, where it has been shown that while numerical values of these quantities may vary with gauge choice, the qualitative features of the phase transition and order-of-magnitude estimates of the resulting gravitational wave signals remain relatively robust. A fully gauge-invariant treatment would require the use of Nielsen identities or other gauge-invariant approaches, which is beyond the scope of the present work. We therefore interpret our results with this inherent theoretical uncertainty in mind. For detailed discussions, see Refs. [113,127–136].

C. Gravitational wave spectrum

First-order phase transition in the early Universe could generate gravitational wave signals observable today. There are three different sources of gravitational waves produced in the first-order phase transitions: bubble wall collisions [137], sound waves [34], and magnetohydrodynamic (MHD) turbulence [138] in the plasma, i.e., the total gravitational wave strength is given by the sum of these as

$$\Omega_{\rm GW}h^2 \simeq \Omega_{\rm sw}h^2 + \Omega_{\rm turb}h^2 + \Omega_{\rm coll}h^2. \quad (45)$$

In order to calculate the contribution from each of these sources, we need to distinguish between three different scenarios of bubble dynamics: runaway, nonrunaway, and runaway in vacuum [125,139]. Depending on the strength of interaction of the bubble wall with the plasma after nucleation, bubbles can either accelerate to attain a terminal velocity before collisions take place (nonrunaway) [139] or keep accelerating to reach approximately the speed of light (runaway) [125,139]. For super-strong phase transitions, plasma effects can be neglected and the walls reach the speed of light (runaway in vacuum). In the case of runaway bubbles, collisions play the dominant part in the GW spectrum because the bubble walls collide at nearly the speed of light. In a nonrunaway scenario, sound waves in the plasma mostly contribute to the total GW spectrum since the wall velocities are small. The distinction between runaway and nonrunaway scenarios is made by comparing the α parameter with the α_∞ parameter, defined as [125,139],

$$\alpha_\infty \simeq \frac{30}{24\pi^2}\frac{1}{g_* T_n^2}\sum_a c_a \Delta m_a^2, \quad (46)$$

where the sum runs over particle species that are light in the symmetric phase and become heavy after the transition. Here Δm_a^2 denotes the corresponding mass-squared difference, and the coefficient c_a equals N_a for bosons and $N_a/2$ for fermions, with N_a being the number of degrees of freedom. We take $g_* \simeq 106.75$ at $T \sim T_n$.

In our model, the parameter α is typically smaller than α_∞ within the viable FOPT region, corresponding to nonrunaway bubble dynamics. However, near the supercooled limit, α exceeds α_∞, indicating a transition to the runaway regime where bubble collisions significantly contribute to the GW spectrum. Supercooled phase transitions produce GW amplitudes that are orders of magnitude larger than those in the nonsupercooled case, leading to substantially higher signal-to-noise ratios (SNR). Consequently, from a detection standpoint in future GW observatories, the

runaway scenario dominates, with bubble collisions providing the primary contribution to the GW signal.

1. Bubble collisions

Assuming the *envelope approximation* [140], the contribution from bubble collision is given by [141–143],

$$h^2\Omega_{\rm env}(f) = 1.67\times10^{-5}\left(\frac{H_*}{\beta}\right)^2\left(\frac{\kappa_c\alpha}{1+\alpha}\right)^2\left(\frac{100}{g_*}\right)^{\frac{1}{3}} \times\left(\frac{0.11v_w^3}{0.42+v_w^2}\right)\frac{3.8(f/f_{\rm env})^{2.8}}{1+2.8(f/f_{\rm env})^{3.8}} \quad (47)$$

where $H_* = H(T_n)$ and the efficiency factor κ_c is given by [144],

$$k_{\rm c} = \frac{0.715\alpha+\frac{4}{27}\sqrt{\frac{3\alpha}{2}}}{1+0.715\alpha} \quad (48)$$

In the above equation, v_w is the wall velocity, which we assume to be unity for calculations. The peak frequency is given by

$$f_{\rm env} = 16.5\times10^{-6}\left(\frac{0.62}{1.8-0.1v_w+v_w^2}\right)\left(\frac{\beta}{H_*}\right) \times\left(\frac{T_n}{100\ {\rm GeV}}\right)\left(\frac{g_*}{100}\right)^{\frac{1}{6}}{\rm Hz} \quad (49)$$

2. Sound waves

The movement of the domain walls (DWs) through the plasma creates pressure waves in the plasma. The contribution of such sound waves to GW is given from numerical fit [141,145,146],

$$h^2\Omega_{\rm sw}(f) = 2.65\times10^{-6}\left(\frac{H_*}{\beta}\right)\left(\frac{\kappa_{sw}\alpha}{1+\alpha}\right)^2\left(\frac{100}{g_*}\right)^{\frac{1}{3}}v_w \times\left(\frac{f}{f_{\rm sw}}\right)^3\left(\frac{7}{4+3(f/f_{\rm sw})^2}\right)^{7/2}\Upsilon \quad (50)$$

where v_w is the wall velocity which we assume as [147],

$$v_w = \begin{cases}\sqrt{\frac{\Delta V(Tn)}{\alpha\rho_{\rm rad}}}, & \text{if } \sqrt{\frac{\Delta V(Tn)}{\alpha\rho_{\rm rad}}} \le v_J\\ 1, & \text{otherwise}\end{cases} \quad (51)$$

where v_J is the Jouguet velocity, $v_J = \frac{1}{\sqrt{3}}\frac{1+\sqrt{3\alpha^2+2\alpha}}{1+\alpha}$. The efficiency factor κ_{sw} is given by [148,149],

$$\kappa_{\rm sw} = \begin{cases}\frac{\alpha}{0.73+0.083\sqrt{\alpha}+\alpha}, & \text{if } v_w \ge v_w^\alpha\\ \frac{6.9\alpha v_w^{6/5}}{1.36-0.037\sqrt{\alpha}+\alpha}, & \text{if } v_w < v_w^\alpha\end{cases} \quad (52)$$

where,

$$v_w^\alpha = \left[\frac{1.36-0.037\sqrt{\alpha}+\alpha}{6.9(0.73+0.083\sqrt{\alpha}+\alpha)}\right]^{5/6} \quad (53)$$

Lastly the factor $\Upsilon = 1-\frac{1}{\sqrt{1+2\tau_{sw}H_*}}$ is a suppression factor dependent on lifetime of sound waves τ_{sw} [146]. It can be parametrized by writing $\tau_{sw}\sim R_*/\bar{U}_f$, where $R_* = (8\pi)^{1/3}v_w/\beta$ and $\bar{U}_f = \sqrt{3\kappa_{\rm sw}\alpha/4}$ represents mean bubble distance and root-mean-squared fluid velocity [150]. The peak frequency is given by,

$$f_{\rm sw} = \frac{1.9\times10^{-5}}{v_w}\left(\frac{\beta}{H_*}\right)\left(\frac{T_*}{100\ {\rm GeV}}\right)\left(\frac{g_*}{100}\right)^{\frac{1}{6}}{\rm Hz} \quad (54)$$

3. Magnetohydrodynamic turbulence

The contribution of turbulent motion in a fully ionized plasma to the gravitational wave (GW) spectrum is described by magnetohydrodynamic (MHD) modeling [141,151,152],

$$h^2\Omega_{\rm turb}(f) = 3.35\times10^{-4}\left(\frac{H_*}{\beta}\right)\left(\frac{\kappa_{\rm turb}\alpha}{1+\alpha}\right)^{\frac{3}{2}}\left(\frac{100}{g_*}\right)^{1/3}v_w \times\frac{(f/f_{\rm turb})^3}{[1+(f/f_{\rm turb})]^{\frac{11}{3}}(1+8\pi f/h_*)} \quad (55)$$

where the turbulence efficiency factor is given by $\kappa_{\rm turb} = 0.05\kappa_{\rm turb}$ [149]. The characteristic frequency scale is expressed as,

$$h_* = 16.5\times10^{-6}\left(\frac{T_n}{100\ {\rm GeV}}\right)\left(\frac{g_*}{100}\right)^{1/6}{\rm Hz} \quad (56)$$

The peak frequency is given by,

$$f_{\rm turb} = \frac{2.7\times10^{-5}}{v_w}\left(\frac{\beta}{H_*}\right)\left(\frac{T_*}{100\ {\rm GeV}}\right)\left(\frac{g_*}{100}\right)^{\frac{1}{6}}{\rm Hz} \quad (57)$$

Figure 2 shows the GW spectrum from FOPT for the four benchmark points with $v_B\sim\mathcal{O}(1)-\mathcal{O}(100)$ TeV, as given in Table III. The colored regions and lines show the sensitivity curves for various future GW experiments. We find that the peak GW frequency from this model in the considered parameter space is expected to be in the mHz-DeciHz range, detectable in experiments such as BBO [101], LISA [99,153], DECIGO, U-DECIGO [100,101], ET [104,105], CE [154,155] etc.

Gravitational waves contribute to the Universe's energy density as dark radiation, constrained by big bang nucleosynthesis (BBN) and cosmic microwave background (CMB) observations through $\Delta N_{\rm eff}$. The bound on the GW energy density is given by,

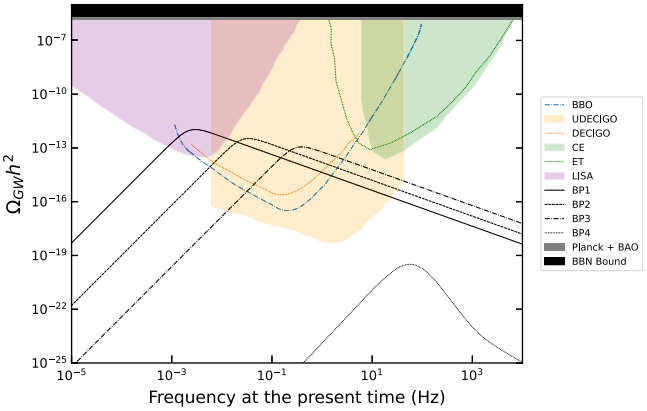


FIG. 2. GW spectra as seen today for benchmark points given in Table III and IV along with noise curves of future GW experiments.

$$\int_{f_{\min}}^{\infty} \frac{df}{f} \Omega_{\rm GW}(f)h^2 \leq 5.6 \times 10^{-6} \Delta N_{\rm eff}, \tag{58}$$

A simplification of the above condition is $\Omega_{\rm GW} \leq 5.6 \times 10^{-6} \Delta N_{\rm eff}$. Figure 2 shows BBN ($\Delta N_{\rm eff}^{\rm BBN} \simeq 0.4$ [156]) and Planck + BAO constraints ($\Delta N_{\rm eff}^{\rm Planck+BAO} \simeq 0.28$ [2]). Future experiments like CMB-HD [157], CMB-Bharat [158], CMB-S4 [159] and NASA's PICO project [160] aim for tighter limits $\Delta N_{\rm eff}^{\rm Proj.} = 0.014$, 0.05 and 0.06 respectively.

The detection feasibility of the GW signal at an experiment is evaluated using the signal-to-noise ratio (SNR) defined by,

$$\text{SNR} = \sqrt{\tau \int_{f_{\min}}^{f_{\max}} \mathrm{d}f \left(\frac{\Omega_{\rm GW}(f)h^2}{\Omega_{\rm exp}(f)h^2} \right)^2}, \tag{59}$$

where $\tau = 4$ years and $f_{\min}$, $f_{\max}$ are the detector's frequency range. A signal is considered detected if SNR ≥ 10.

We end this section by mentioning that in our setup, local cosmic strings will form when $U(1)_B$ is broken to Z_2, and contribute to the GW spectra [161–167]. However, such GW signals are highly suppressed for symmetry breaking scales $v_B \sim 10^4$–10^5 GeV. The string tension is given by $\mu \simeq 2\pi v_B^2$, leading to a dimensionless parameter $G\mu \simeq 2\pi v_B^2/M_{\rm Pl}^2 \sim 10^{-30} - 10^{-28}$. The resulting stochastic GW background from a scaling network of local cosmic strings is approximately flat with amplitude [161,167–169]

$$\Omega_{\rm GW}^{\rm CS} h^2 \sim 10^{-2} \Omega_r h^2 \sqrt{\alpha G\mu} \sim 10^{-7} \sqrt{G\mu} \sim 10^{-22} - 10^{-21}, \tag{60}$$

where $\Omega_r h^2 \simeq 4.2 \times 10^{-5}$ and $\alpha \sim 0.1$. The characteristic frequency today is set by the formation temperature $T_{\rm form} \sim v_B$,

$$f_{\rm CS} \sim 10^{-3}\ \text{Hz} \left(\frac{T_{\rm form}}{100\ \text{GeV}} \right) \sim 0.1\text{–}1\ \text{Hz}. \tag{61}$$

In contrast, a supercooled FOPT at the same scale, leading to runaway bubbles, produces a significantly stronger GW signal, as shown in Fig. 2. Here, BP1–BP3 correspond to runaway cases, while BP4 represents a nonrunaway scenario with a GW amplitude comparable to that from cosmic strings. Since detectable SNRs in our analysis predominantly arise from runaway scenarios, we conclude that for $v_B \sim 10^4$–10^5 GeV,

$$\Omega_{\rm GW}^{\rm CS} \ll \Omega_{\rm GW}^{\rm FOPT}, \tag{62}$$

indicating that the GW contribution from local cosmic strings is negligible compared to that from the FOPT across all relevant frequencies.

TABLE III. Benchmark points for strong FOPT. The calculated GW parameters for these benchmark points are given in Table IV and the corresponding GW signals are plotted in Fig. 2.

	BP1	BP2	BP3	BP4
λ_{HS}	0.01	0.01	0.01	0.01
v_B (TeV)	3.84	19.28	165.24	105.22
m_S (TeV)	0.219	1.1374	10.3687	5.151
$m_{Z'}$ (TeV)	2.493	12.344	117.52	39.43
m_χ (TeV)	1.246	6.1719	58.7	19.72
m_ψ (TeV)	1.50	7.304	67.3	43.67
m_ξ (TeV)	1.275	6.409	81.390	42.37

IV. CURRENT BOUNDS

A. Electroweak precision bounds

Electroweak precision observables provide key insights into potential new physics beyond the SM [170–172]. A powerful tool for capturing these effects is the *STU* formalism [171], which expresses deviations in gauge boson self-energies through three oblique parameters: S measures the impact of new physics on neutral current interactions at different energy scales, T quantifies the relative shift in neutral versus charged current processes, linked to the ρ parameter and U captures additional effects on charged currents but is typically small. These parameters are defined as [173],

$$\alpha S = 4s^2c^2 \frac{\Pi_Z(m_Z^2) - \Pi_Z(0)}{m_Z^2}, \tag{63}$$

$$\alpha T = \frac{\Pi_W(0)}{m_W^2} - \frac{\Pi_Z(0)}{m_Z^2}, \tag{64}$$

$$\alpha(S+U) = 4s^2 \frac{\Pi_W(m_W^2) - \Pi_W(0)}{m_W^2}, \tag{65}$$

where s and c are the sine and cosine of the weak mixing angle and α is the fine structure constant, all evaluated at m_Z. The latest global fit from the Particle Data Group (2024) [174] constrains these parameters as follows:

$$S = -0.04 \pm 0.10, \quad T = 0.01 \pm 0.12, \quad U = -0.01 \pm 0.09. \tag{66}$$

We evaluate S, T, and U across various parameter points using SPHENO [175], identifying regions of parameter space that remain consistent with these bounds within 1σ.

B. DM direct detection

In this section, we examine the constraints imposed by direct detection experiments on the viable parameter space of our DM model. These experiments are designed to probe potential interactions between DM particles and detector nuclei, typically resulting in measurable nuclear recoil signals. The relevant observable in this context is the spin-independent DM-nucleon scattering cross section, σ_{SIDD}, which we compute as a function of the DM mass m_{Ψ_1}.

In our model, the dark matter candidate interacts with nucleons primarily through processes mediated by Z', s and the SM Z boson. However, the contributions from the Z' and s exchanges are suppressed due to the large masses appearing in their propagators, with the suppression becoming more pronounced as the $U(1)_B$ symmetry-breaking scale v_B increases. Consequently, the dominant contribution arises from the Z-mediated interactions (for more details see Ref. [88]), where the scattering cross section is governed by the mixing angle $\sin\theta_{\mathrm{DM}}$, which controls the singlet-doublet composition of the dark matter candidate. This makes Z-mediated processes particularly relevant for potential signatures in direct detection experiments. The detailed expressions for the tree-level SIDD cross section for a fermionic DM can be found in [20,21,93,176]. These interactions are sensitive to the mixing angle and mass spectrum of the exotic fermions, which also influence the thermal relic abundance. For our analysis, we employ the MICROMEGAS [177] framework, which incorporates nuclear form factors and astrophysical inputs to evaluate σ_{SIDD}.

In Fig. 3, we plot σ_{SIDD} as a function of m_{Ψ_1} for representative values of the input parameters, along with current direct detection bounds from PandaX-4T (2025) [178], LUX-ZEPLIN (LZ) (2025) [179] and XENONnT (2025) [180]. The most stringent bound comes from LZ (2025). The effects of λ_{HS} and θ_{DM} are shown. We see that for $\theta_{\mathrm{DM}} = 0.001$, the DM candidate is predominantly singletlike, suppressing its interactions with nucleons mediated by the SM Z boson. This results in lower cross section values, with most of the parameter points lying below the experimental bounds. In contrast, for $\theta_{\mathrm{DM}} = 0.03$, the DM candidate acquires a larger doublet component, significantly enhancing its Z-mediated interactions with nucleons. This leads to a notable increase in the cross section for large θ_{DM}, causing DM candidates with masses below 1400 GeV to be ruled out by LZ (2025). For smaller values of θ_{DM}, LZ (2025) establishes a lower bound on the mass m_{Ψ_1}. In our random parameter scan, we implement this bound on our DM candidate. We also see that for a larger value of λ_{HS}, the cross section is generally larger, which is expected since a larger coupling means a stronger mixing between DM and nucleons via scalar exchange, which in turn enhances the cross section.

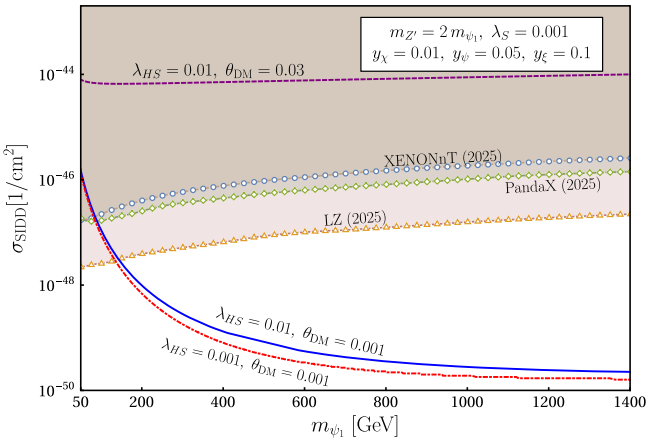


FIG. 3. Direct detection bounds from PandaX-4T (2025), LUX-ZEPLIN (2025) and future projection for XENONnT (2025) plotted along with σ_{SIDD} calculated for our DM candidate for various values of model parameters. Here we assume the resonant condition $m_{Z'} = 2m_{\Psi_1}$.

C. DM indirect detection

Indirect detection of DM involves searching for SM particles produced in its annihilation or decay [181]. In the context of our model, the DM candidate is a Dirac-type fermion. Unlike Majorana DM scenarios, where final state radiation (FSR) is typically suppressed, Dirac-type DM produces a continuous gamma-ray spectrum rather than distinct monochromatic gamma-ray lines [182]. As a result, searching for a sharp gamma-ray signature is challenging and the focus shifts to analyzing diffuse gamma-ray emissions arising from dark matter annihilation in astrophysical environments.

In our model, the dominant annihilation channels proceed via the exchange of the Z' boson, leading to final states that predominantly include quark-antiquark pairs (e.g., $b\bar{b}$, $t\bar{t}$) and gauge bosons (W^+W^-), or leptons ($\tau\bar{\tau}$). Figures 4 and 5 shows example processes. These annihilation products contribute to the diffuse gamma-ray flux observed by current experiments such as *Fermi-LAT* [183–186], *H.E.S.S.* [187,188] and next-generation observatory *CTA* [189,190]. These experiments provide stringent constraints on the thermally averaged annihilation cross section $\langle\sigma v\rangle_{\mathrm{ann}}$

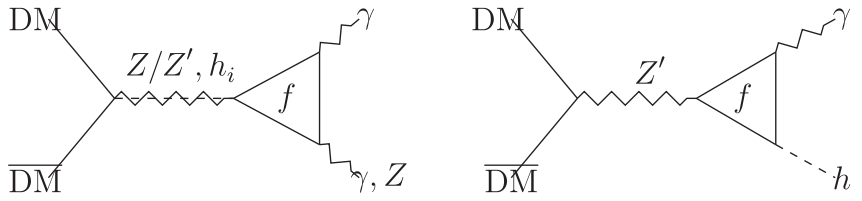


FIG. 4. Loop-induced annihilation of dark matter particles into monochromatic photons through the processes $\mathrm{DM}\overline{\mathrm{DM}} \to \gamma\gamma, \gamma Z$ and γh in a generic BSM framework featuring an exotic gauge boson mediator (Z'). The internal fermion f represents either a Standard Model fermion or an exotic fermionic state predicted by the model.

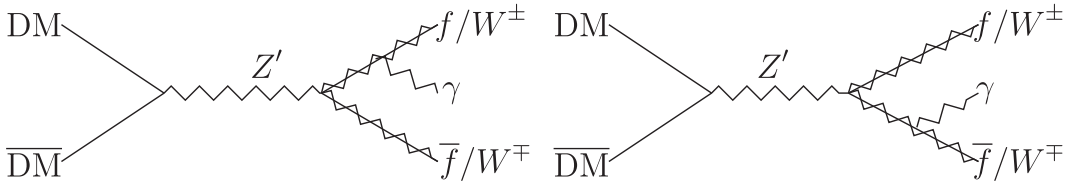


FIG. 5. Tree-level annihilation channels of dark matter leading to the production of diffuse gamma-ray signals. In these processes, the final state includes fermion pairs $f\bar{f}$, where f may be a Standard Model or an exotic fermion predicted by the model.

of the DM. We use MICROMEGAS to calculate the annihilation cross section as a function of DM mass.

In Fig. 6, we show $\langle\sigma v\rangle_{\mathrm{ann}}$ for different final state annihilation channels, namely $b\bar{b}$, $\tau^+\tau^-$ and W^+W^-, for various becnchmark paramater points. Current bounds from *Fermi-LAT*, *H.E.S.S* and future projection from *CTA* are shown. The left and right columns corresponds to $\theta_{\mathrm{DM}} = 0.001$ and 0.03 respectively. Other parameter values are mentioned in the caption. We see that the given benchmark point is not ruled out by indirect detection experiments. The $b\bar{b}$ annihilation cross section shows a narrow peak at the Z' resonance, however, not reach the sensitivity of *H.E.S.S.* for the given parameter point. A thorough analysis of the annihilation cross section near the Z' resonance is required for a more definitive assessment of indirect constraints but is beyond the scope of this work. Overall, much of the DM parameter space in our model remains unconstrained by current indirect detection limits, though the $\Psi_1\Psi_1 \to b\bar{b}$ channel may be further tested by future experiments.

D. Collider bounds

Collider experiments such as LEP and LHC provide stringent constraints on the parameter space of $U(1)_B$. In particular, the new gauge boson Z' can be produced via quark-antiquark annihilation at colliders, which subsequently decays into a pair of leptons or jets. The strongest bounds arise from LHC searches for narrow resonances in the dilepton (e^+e^-, $\mu^+\mu^-$) and dijet final states. These analyses set lower limits on the Z' mass $m_{Z'}$ as a function of the gauge coupling g_B. We utilize the results presented in [88], which are derived from the analyses performed in [191–194], valid in the mass range $m_{Z'} \in [500, 1800]$ GeV. This study assumes Ψ_1^+ to be the heaviest among the four exotic fermionic states. Accordingly, we restrict our parameter space by adopting the hierarchy $y_\xi \gg y_\psi \gg y_\chi$. While broadly consistent, these constraints may differ slightly due to the inclusion of mixing between the singlet and doublet exotic fermions in our setup.

In addition to the bounds on $m_{Z'}$ and g_B, the exotic fermion masses are also constrained from compressed MSSM search at ATLAS [88,193]. The ATLAS analysis sets a 95% CL upper bound on the production cross section of wino/binolike chargino-neutralino pairs, which has been conservatively reinterpreted to constrain the $U(1)_B$ model by mapping the $\Psi_2^\pm\Psi_2$ production to the chargino-neutralino topology, projecting limits in the $m_{\Psi_2^\pm} = m_{\Psi_2}$ vs. $\Delta M(\Psi_2, \Psi_1)$ plane. The detailed analysis and plots of these bounds are given in [88]. These bounds are taken into account while scanning the parameter space of the model in Fig. 7 later.

In our model, the new charged fermions $\Psi^\pm$ and $\xi^\pm$ contribute to the $h \to \gamma\gamma$ decay amplitude at one loop. The total amplitude can be expressed as [195–197],

$$\mathcal{A}(h \to \gamma\gamma) = A_W + A_t + \sum_F A_F, \tag{67}$$

where A_W and A_t denote the SM W-boson and top-quark loop contributions, respectively, and A_F represents the contribution of a charged BSM fermion F. For a heavy fermion F with mass $m_F \gg m_h$, the contribution simplifies to [195,196,198],

$$A_F \simeq N_c Q_F^2 \frac{y_F v}{m_F} \cdot \frac{4}{3}, \tag{68}$$

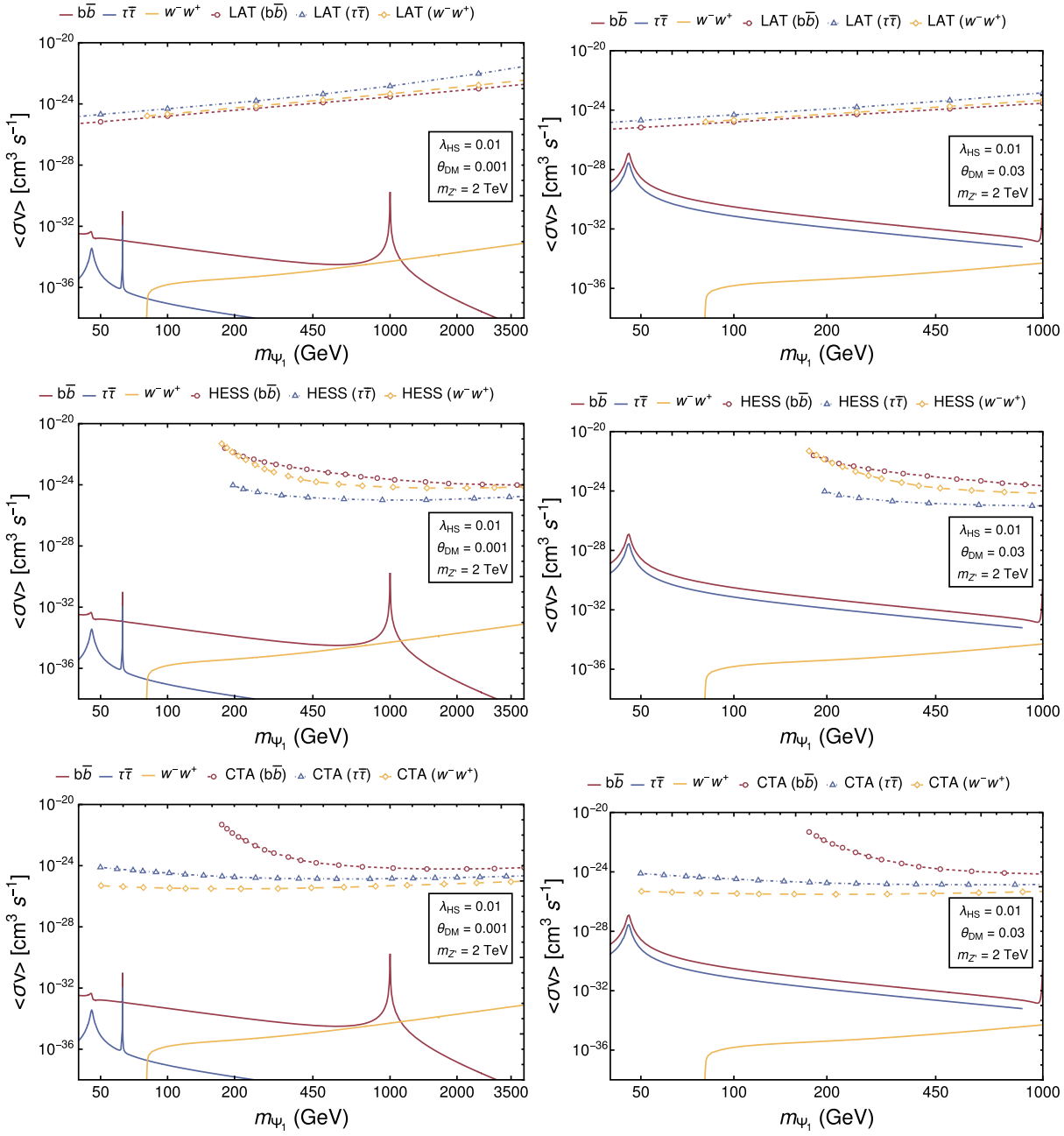


FIG. 6. Indirect detection constraints on the thermally averaged annihilation cross section $\langle\sigma v\rangle_{\rm ann}$ as a function of the dark matter mass m_{Ψ_1}, for various annihilation channels. Current and projected upper limits from Fermi-LAT, H. E. S. S. and CTA observations based on diffuse gamma-ray measurements are also shown. The benchmark parameters used are $\theta_{\rm DM} = 0.001$ (left column) and $\theta_{\rm DM} = 0.03$ (right column). Other parameters we consider are $\lambda_{HS} = 0.01, \lambda_S = 10^{-3}, m_{Z'} = 2$ TeV, $y_\chi = 0.01, y_\psi = 0.05, y_\xi = 0.1$.

where N_c is the color factor, Q_F is the electric charge of the fermion, y_F is its Yukawa coupling to the Higgs, and $v = 246$ GeV is the SM Higgs vacuum expectation value. Numerically, for the SM contributions, one has [195,199],

$$A_W \approx -8.3, \qquad A_t \approx +1.8, \qquad A_{\rm SM} = A_W + A_t \approx -6.5. \tag{69}$$

The charged fermion masses are primarily generated from the $U(1)_B$ breaking scale v_B,

$$m_F \simeq y_F v_B, \tag{70}$$

so that the ratio controlling the Higgs coupling to these fermions is

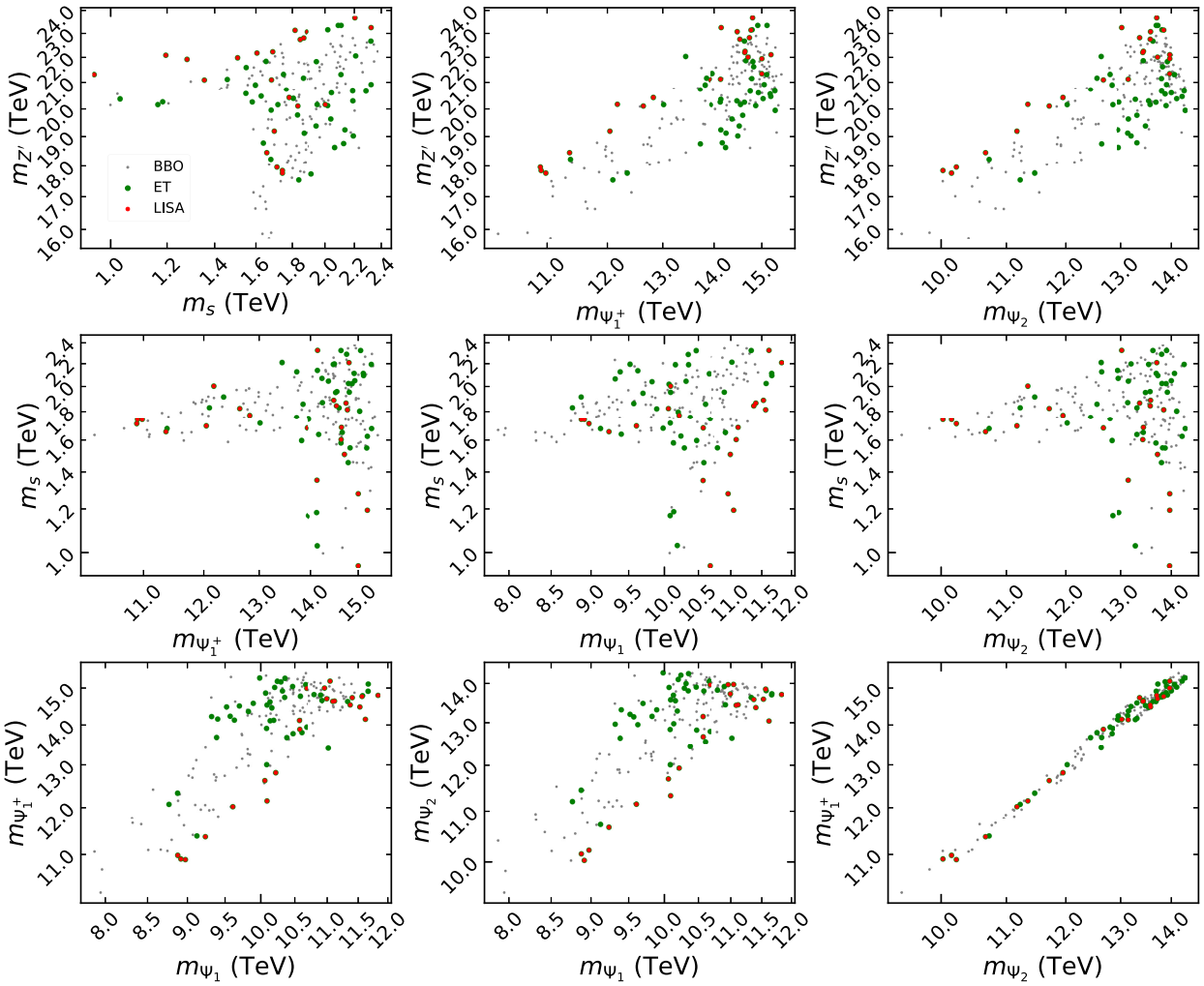


FIG. 7. SNR > 10 points with $\lambda_{HS} = 0.01$ calculated for future GW experiments BBO, LISA and ET. Here, all the points satisfy the relic abundance bound of dark matter, constraints on oblique parameters from electroweak precision experiments within 1σ range, current collider bounds and DM direct detection bounds. This plot shows the correlation among various physical masses of the model, accessible to future GW and laboratory experiments.

$$\frac{y_F v}{m_F} \simeq \frac{v}{v_B}. \tag{71}$$

For the range of v_B relevant for our analysis, $v_B \sim 10^4$–10^5 GeV, this ratio varies between

$$\frac{v}{v_B} \sim 2.5 \times 10^{-3} \text{ to } 2.5 \times 10^{-2}, \tag{72}$$

leading to BSM contributions to the amplitude

$$A_F \sim \mathcal{O}(10^{-2} - 10^{-1}), \tag{73}$$

which remain much smaller than the SM amplitude $A_{\rm SM} \sim -6.5$. Consequently, the shift in the Higgs diphoton signal strength,

$$\mu_{\gamma\gamma} = \frac{|\mathcal{A}_{\rm SM} + \sum_F A_F|^2}{|A_{\rm SM}|^2} \simeq 1 + \mathcal{O}(10^{-3} - 10^{-2}), \tag{74}$$

remains below the current experimental sensitivity. The latest combined ATLAS and CMS measurement gives [199],

$$\mu_{\gamma\gamma} = 1.04 \pm 0.07, \tag{75}$$

corresponding to a few-percent level precision. Even at the lower end $v_B \sim 10^4$ GeV, the BSM contributions are at most ∼1%, still below experimental sensitivity. This demonstrates that, in the parameter space considered, the new charged fermion contributions effectively decouple and do not impose any additional constraint on the Higgs diphoton decay. Therefore, we do not include the $h \to \gamma\gamma$ constraint explicitly in our numerical scans.

Future high-energy experiments will significantly enhance the sensitivity to this model across multiple channels. The HL-LHC will probe leptophobic Z' bosons up to several TeV [200–202], while searches for compressed electroweak fermions with soft leptons or disappearing tracks will constrain the $m_{\Psi_1} - \Delta M$ plane up to nearly 500 GeV [203]. FCC-hh will extend the Z' mass reach to ∼30 TeV [204] and lepton colliders like ILC will be sensitive to low-mass compressed states with high precision [205]. Long-lived particle (LLP) detectors like MATHUSLA [206,207] and FASER [208–210] can also put constraints in the parameter space of the model. Finally, low-energy observables like parity violation (MOLLER, P2) and rare meson decays (NA62, KOTO) will test $m_{Z'}/g_B > 10$ TeV [211–214]. These diverse and complementary probes make this an exceptionally testable and exciting model in upcoming experimental programs.

V. NUMERICAL ANALYSIS

In this section, we discuss the parameter scan of the model and the results obtained. We modified the packages TRANSITIONLISTENER[1] [215] and COSMOTRANSITIONS[2] [216] to evaluate the phase transition parameters for different values of model parameters. We consider the free parameters in this model: $v_B, \lambda_S, g_B, y_\chi, y_\psi, y_\xi, \lambda_{HS}$, $\sin\theta_{\rm DM}, \sin\theta_p$ and derived parameters: $m_s, m_{Z'}, m_{\Psi_1}, m_{\Psi_2}$, $m_{\Psi_1^+}, m_{\Psi_2^+}, \sin\theta, M_2, M_4$. The nature of the phase transition does not depend on the parameters $\sin\theta_{\rm DM}$ and $\sin\theta_p$; however, they affect DM phenomenology. First, we scan the following parameter space of our model for phase transition analysis,

$$v_B \in [10^3, 10^6]\ \text{GeV}, \qquad \lambda_S \in [10^{-4}, 1],$$
$$g_B \in [10^{-4}, 1], \qquad y_{\chi,\psi,\xi} \in [10^{-4}, 1] \tag{76}$$

along with the imposed condition: $y_\xi \gg y_\psi \gg y_\chi$ such that Ψ_1 is the DM candidate and Ψ_1^+ is heaviest, as discussed earlier. We fix the value for $\lambda_{HS} = 0.01$ (see Appendix B for details), which is related to scalar mixing $\sin\theta$. Additionally, as discussed in Appendix A, we consider the resonant condition on the DM mass $m_{\Psi_1} \sim m_\chi = m_{Z'}/2$ in order to not overproduce dark matter, which is valid for small $\sin\theta_{\rm DM}$ values. We are interested in strong first-order phase transitions (SFOPT), which could give observable GW signals. We generate random parameter points within the given limits above and calculate different PT and GW parameters. We take $\sin\theta_p = 0$ as discussed earlier.

We randomly generate around 20000 parameter points resulting in an FOPT. We make sure that each chosen point satisfies the conditions for the stability of the scalar potential given in Eq. (12) and perturbativity limits given in Eq. (13). Moreover, as described in Sec. III A, we also make sure that the effective potential is bounded from below. Additionally, we also consider the running of the couplings in the model (see Appendix B for RGEs) and accept parameter points only if they keep the Higgs potential stable and do not hit the Landau pole upto Planck scale. Out of the total number of random parameter points, we show 3 benchmark points (BP1, BP2, BP3, BP4) in Table III in terms of the physical masses. We show the example GW spectra for these benchmarks in Fig. 2, where we use the calculated phase transition parameters given in Table IV.

TABLE IV. Phase transition parameters calculated for the benchmark points for FOPT given in Table III. The GW signals for these benchmark points are plotted in Fig. 2.

	BP1	BP2	BP3	BP4
T_c/GeV	407.54	2183.25	19451.33	16948.20
T_n/GeV	72.38	699.48	7965.24	16552.45
v_c/T_c	9.42	8.83	8.49	3.35
α	49.96	3.90	1.55	0.00922
α_∞	0.01	0.02	0.019	0.011304
β/H_*	976.01	1196.44	1251.48	17448.24
$\sqrt{\frac{\Delta V(Tn)}{\alpha\rho_{\rm rad}}}$	0.91	0.94	1.0	0.94
v_J	0.99	0.98	0.95	0.650
v_w^α	0.199	0.214	0.233	0.331

For DM phenomenology, we consider the same random points obtained in the above parameter scan and evaluate them considering two values for the DM mixing: $\sin\theta_{\rm DM} = 0.001$ and 0.03. The charged sector mixing $\sin\theta_p$ is considered to be 0 as discussed earlier. With these values, we implement our model in SARAH [217], SPHENO [218], and MICROMEGAS [177] to calculate the particle spectra and the DM relic abundance. For each of the parameter points, in addition to the DM relic density, we calculate S, T, U parameters and $\sigma_{\rm SIDD}$ discussed in Sec. IV. We impose electroweak precision bounds on S, T, U parameters within 1σ confidence level, DM relic density bound $\Omega_{\Psi_1}h^2 \lesssim 0.12$ and DM direct detection bounds from LUX-ZEPLIN (2025). We do not consider the indirect detection bounds, as they require more careful study. We also impose the current collider bounds on the parameter points coming from LHC described in Sec. IV.

Finally, in Fig. 7, we show the viable parameter space of our model that satisfies all the theoretical and current experimental constraints, at the same time generating strong GW signals to be detected in future GW experiments such as LISA, ET and BBO. This parameter space will be sensitive to future GW, collider and DM experiments, demonstrating the complementarity of these experiments to probe this model. We showcase the viable parameter space as correlations among masses of various physical

[1] https://github.com/tasicarl/TransitionListener.
[2] https://github.com/clwainwright/CosmoTransitions.

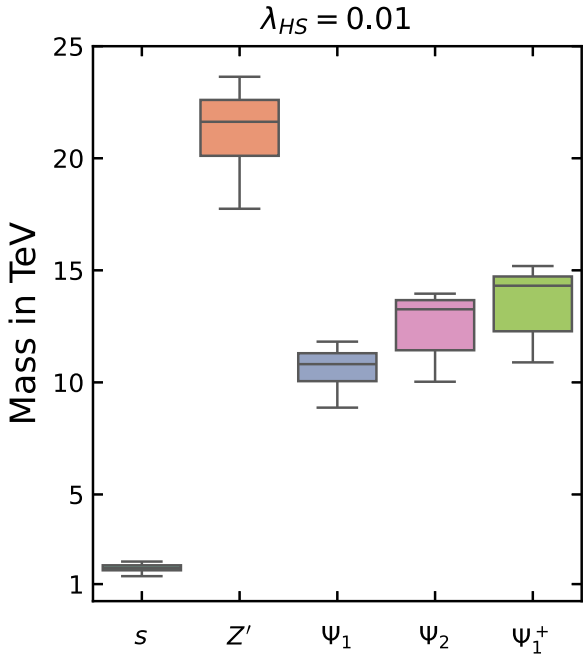


FIG. 8. Box plots of physical masses for the parameter points shown in Fig. 7. The colored boxes span the inter-quartile range (IQR) of the parameter points, the horizontal lines inside the boxes mark the median and the whiskers extend to the most extreme values within $1.5 \times$ IQR. The diagrams summarise the typical mass scales realized by the viable parameter space of the model, which satisfies all the current theoretical and experimental constraints and can be probed in future collider studies as well as GW detectors.

states in the model. The gray, green, and red points are sensitive in BBO, ET and LISA, respectively, with SNR > 10, implying 5σ C.L. of detection. For this figure, we consider $\lambda_{HS} = 0.01, \sin\theta_{\rm DM} = 0.001$. We find that taking $\sin\theta_{\rm DM} = 0.03$ does not change the plots significantly.

In Fig. 8, we show box plots of the physical masses of the model. These plots summarize the distribution of viable physical masses within the model, displaying the median, interquartile range (IQR) and potential outliers. The box spans from the 25th to the 75th percentiles, with the central line indicating the median. Whiskers extend to data points within 1.5 times the IQR from the lower and upper quartiles. Points beyond this range are considered as outliers. These box plots are created considering the parameter points in Fig. 7 and they exhibit the statistics of the particle spectra satisfying all the current bounds discussed above and producing strong GW signals detectable at future GW observatories. Future colliders and DM detection experiments can shed light on the same parameter space, thereby complementing GW observations. In general, we find that DM mass m_{Ψ_1} around 8–12 TeV, Z' mass around 16–24 TeV and new scalar mass m_s around 1–2.5 TeV can be most interesting to test in the future GW, DM direct detection and collider experiments in synergy. Anything below these mass scales are ruled out primarily by LZ 2025 results while dark matter above ~12 TeV will not be detectable in LISA, BBO, and ET.

VI. CONCLUSION AND DISCUSSION

We considered a minimal extension of the SM where baryon number is gauged with a $U(1)_B$ group. The anomaly cancellation is ensured by introducing new fermions with nonzero baryonic charges, such as χ (electric charge neutral and SM singlet), Ψ ($SU(2)_L$ doublet and nonzero hypercharge), and ξ (electrically charged and isospin singlet) to the particle content of the SM. These new fermions mix and give rise to four physical states Ψ_1, Ψ_2, Ψ_1^+, and Ψ_2^+, where the lightest Ψ_1 is found to be a stable dark matter candidate. Additionally, we add a complex scalar S to break the $U(1)_B$ symmetry.

We studied the dynamics of the phase transition in this prescribed framework. We considered the effective potential including one-loop Coleman-Weinberg corrections, counterterms to renormalize the potential, thermal corrections, and daisy-resummation. Numerically, we examined various benchmark points leading to strong first-order phase transitions, which produce GWs through collisions and movements of nucleated bubbles in the thermal plasma of the early Universe. We have also checked the thermal relic abundance of dark matter and showed that in the resonance region $m_{\Psi_1} \sim m_{Z'}/2$, the DM satisfies the observed relic conditions while consistent with the prediction of gravitational wave signals. Additionally, we discussed constraints on this model from electroweak precision experiments, colliders, DM direct and indirect detection experiments. We also considered the running of the coupling constants of the model by solving the 1-loop renormalization group equations (RGEs) to find parameter values such that the Higgs potential remains stable and none of the couplings hit the Landau pole upto Planck scale. We scanned the parameter space of the model and found viable parameter points that satisfy all the current bounds while producing a strong enough GW signal to be detected in various future GW experiments such as LISA, ET, BBO, DECIGO, etc., with signal-to-noise ratio SNR > 10. Future GW experiments and collider searches can simultaneously probe this viable parameter space and complement astrophysical experiments related to DM direct and indirect detection. We showed the mass distributions of different physical states of our model as correlations in Fig. 7 and as box plots in Fig. 8. We showed that the parameter space of interest naturally favors masses of a few to tens of TeV for dark matter and the Z' boson, while a few TeV masses for the scalar. They emerge as well-motivated targets for next-generation colliders operating at 100 TeV, where both the dark matter and Z' resonances could be probed directly. These findings highlight the complementarity of GW, astrophysical, and collider frontiers in testing gauge-extended dark matter models.

ACKNOWLEDGMENTS

Authors thank Prof. Tao Han and Dr. Arnab Dasgupta for their valuable insights on various aspects of the paper. Taramati is supported by DST-INSPIRE (IF200289) fellowship. L. M. is supported by a UGC fellowship. Z. A. B. is supported by the IoE fund at IIT Bombay.

DATA AVAILABILITY

There are no publicly available research data or software supporting this manuscript. Requests for further information or data should be sent to the authors.

APPENDIX A: RELIC DENSITY OF DARK MATTER

Here, we review the relic abundance of the dark matter candidate Ψ_1 in this model and explain the resonant condition that is considered throughout this paper. Mass hierarchies among Ψ_1, Ψ_2, Ψ_1^+ and Ψ_2^+ influence the relic abundance through self-annihilation and coannihilation channels. Unlike in [50], due to the presence of additional channels in our model, the DM mass need not exceed m_s and $m_{Z'}$ to achieve the correct relic abundance. The cosmological evolution of exotic fermions follows the Boltzmann equation [72],

$$\frac{dn}{dt} + 3\mathcal{H}n = -\langle\sigma v\rangle_{\rm eff}(n^2 - n_{\rm eq}^2), \tag{A1}$$

where $n = n_{\Psi_1} + n_{\Psi_2} + n_{\Psi^+_{1/2}}$. Since we consider $y_\chi \ll y_\psi \ll y_\xi$, the heavier particles $\Psi_2, \Psi_1^+, \Psi_2^+$ decays to the DM particle Ψ_1 such that eventually $n = n_{\Psi_1}$. The effective cross section $\langle\sigma v\rangle_{\rm eff}$ is [88],

$$\begin{aligned}\langle\sigma v\rangle_{\rm eff} = {}& \frac{g_1^2}{g_{\rm eff}^2}\langle\sigma v\rangle_{\overline{\Psi_1}\Psi_1} + \frac{2g_1g_2}{g_{\rm eff}^2}\langle\sigma v\rangle_{\overline{\Psi_1}\Psi_2}\left(1+\frac{\Delta M}{m_{\Psi_1}}\right)^{\frac{3}{2}} e^{-x\frac{\Delta M}{m_{\Psi_1}}} \\ & + \frac{2g_1g_3}{g_{\rm eff}^2}\langle\sigma v\rangle_{\overline{\Psi_1}\Psi_i^+}\left(1+\frac{\Delta M}{m_{\Psi_1}}\right)^{\frac{3}{2}} e^{-x\frac{\Delta M}{m_{\Psi_1}}} \\ & + \frac{2g_2g_3}{g_{\rm eff}^2}\langle\sigma v\rangle_{\overline{\Psi_2}\Psi_i^+}\left(1+\frac{\Delta M}{m_{\Psi_1}}\right)^{3} e^{-2x\frac{\Delta M}{m_{\Psi_1}}} \\ & + \frac{g_2^2}{g_{\rm eff}^2}\langle\sigma v\rangle_{\overline{\Psi_2}\Psi_2}\left(1+\frac{\Delta M}{m_{\Psi_1}}\right)^{3} e^{-2x\frac{\Delta M}{m_{\Psi_1}}} \\ & + \frac{g_3^2}{g_{\rm eff}^2}\langle\sigma v\rangle_{\Psi_i^+\Psi_i^-}\left(1+\frac{\Delta M}{m_{\Psi_1}}\right)^{3} e^{-2x\frac{\Delta M}{m_{\Psi_1}}},\end{aligned} \tag{A2}$$

where $\Delta M = m_{\Psi_2} - m_{\Psi_1}$ is the mass difference between the DM and the next-to-lightest stable particle and $g_{\rm eff}$ is,

$$\begin{aligned}g_{\rm eff} = {}& g_1 + g_2\left(1+\frac{\Delta M}{m_{\Psi_1}}\right)^{3/2} e^{-x\frac{\Delta M}{m_{\Psi_1}}} \\ & + g_3\left(1+\frac{\Delta M}{m_{\Psi_1}}\right)^{3/2} e^{-x\frac{\Delta M}{m_{\Psi_1}}},\end{aligned} \tag{A3}$$

where g_1, g_2, g_3 are the degrees of fredom of Ψ_1, Ψ_2, Ψ_i^+ (where $i = 1, 2$). The final relic abundance [219] is,

$$\Omega_{\Psi_1}h^2 = \frac{1.09\times10^9\ {\rm GeV}^{-1}}{g_*^{1/2}M_{\rm Pl}}\frac{1}{J(x_f)}, \tag{A4}$$

with $J(x_f)$ defined as

$$J(x_f) = \int_{x_f}^{\infty}\frac{\langle\sigma|v|\rangle_{\rm eff}}{x^2}dx. \tag{A5}$$

It is seen that the DM relic abundance is usually above the experimental limit 0.12 for most of the parameter space except at the *resonance* regimes where the mass of DM is approximately half of the mass of the mediator of the annihilation channel. This enhances the annihilation cross section of DM via on-shell production of the mediator. We find in this model that such resonance in the annihilation via Z' mediator allows the DM relic to be within the experimental limit [93,220]. Therefore, in our analysis, we consider the resonant condition $m_{\Psi_1} \sim m_{Z'}/2$ such that the DM does not overclose the Universe.

APPENDIX B: ONE-LOOP BETA FUNCTIONS

The renormalization group equations (RGEs) of a parameter p_i can be written as

$$\frac{dp_i}{dt} = \frac{1}{16\pi^2}\beta_{p_i} \tag{B1}$$

where β_{p_i} is the corresponding beta function and $t = \ln(\frac{\mu}{\rm GeV})$ is the variable related to the renormalization scale μ. We define the threshold step functions for the BSM fields

$$\Theta_\Psi \equiv \theta(\mu - m_\Psi), \qquad \Theta_\xi \equiv \theta(\mu - m_\xi), \qquad \Theta_\chi \equiv \theta(\mu - m_\chi). \tag{B2}$$

For compactness we use the conservative shorthand

$$\Theta_B^{\rm sum} \equiv \Theta_\Psi + \Theta_\xi \tag{B3}$$

where the $+$ operator signifies the *OR* operation. The above factor is multiplied to the $U(1)_B$ (and mixed $U(1)$–$U(1)_B$) pure-gauge contributions to switch them on only when the baryon-charged species are active. The one-loop beta functions for various couplings of the model are given below.

1. Gauge couplings

$$\beta_{g_1}^{(1)} = \frac{1}{10}\Big(16\sqrt{10}g_1^2 g_{BY} + 53g_1^3 + g_1(285g_{BY}^2 + 53g_{YB}^2 + 8\sqrt{10}g_{YB}g_B)(\Theta_B^{\rm sum}) + g_{YB}(285g_B + 8\sqrt{10}g_{YB})g_{BY}(\Theta_B^{\rm sum})\Big), \tag{B4}$$

$$\beta_{g_{YB}}^{(1)} = \frac{1}{10}\Big(g_1^2(53g_{YB} + 8\sqrt{10}g_B)(\Theta_\Psi + \Theta_\xi) + g_1(285g_B + 8\sqrt{10}g_{YB})g_{BY}(\Theta_B^{\rm sum}) + g_{YB}(16\sqrt{10}g_{YB}g_B + 285g_B^2 + 53g_{YB}^2)(\Theta_B^{\rm sum})\Big), \tag{B5}$$

$$\beta_{g_2}^{(1)} = -\frac{5}{2}g_2^3, \tag{B6}$$

$$\beta_{g_3}^{(1)} = -7g_3^3, \tag{B7}$$

$$\beta_{g_B}^{(1)} = \frac{1}{10}\Big(16\sqrt{10}g_{YB}g_B^2 + 285g_B^3 + 53g_{YB}^2 g_B + g_{YB}g_{BY}(53g_1 + 8\sqrt{10}g_{BY}) + g_B g_{BY}(285g_{BY} + 8\sqrt{10}g_1)\Big)(\Theta_B^{\rm sum}), \tag{B8}$$

$$\beta_{g_{BY}}^{(1)} = \frac{1}{10}\big(285g_{BY}(g_B^2 + g_{BY}^2) + 53g_1^2 g_{BY} + 53g_1 g_{YB}g_B + 8\sqrt{10}g_1(2g_{BY}^2 + g_B^2) + 8\sqrt{10}g_{YB}g_B g_{BY}\big)(\Theta_B^{\rm sum}). \tag{B9}$$

2. Scalar quartic couplings

$$\begin{aligned}\beta_{\lambda_H}^{(1)} = {}& \frac{27}{200}g_1^4 + \frac{9}{20}g_1^2 g_2^2 + \frac{9}{8}g_2^4 - \frac{9}{5}g_1^2\lambda_H - \frac{9}{5}g_{YB}^2\lambda_H - 9g_2^2\lambda_H + 24\lambda_H^2 + \lambda_{HS}^2 + 4\lambda_H|y_1|^2\Theta_\Psi + 4\lambda_H|y_2|^2\Theta_\Psi \\ & + 4\lambda_H|y_3|^2\Theta_\Psi + 4\lambda_H|y_4|^2\Theta_\Psi - 2|y_1|^4\Theta_\Psi - 2|y_2|^4\Theta_\Psi - 2|y_3|^4\Theta_\Psi - 2|y_4|^4\Theta_\Psi + 12\lambda_H{\rm Tr}(Y_d Y_d^\dagger) \\ & + 4\lambda_H{\rm Tr}(Y_e Y_e^\dagger) + 12\lambda_H{\rm Tr}(Y_u Y_u^\dagger) - 6{\rm Tr}(Y_d Y_d^\dagger Y_d Y_d^\dagger) - 2{\rm Tr}(Y_e Y_e^\dagger Y_e Y_e^\dagger) - 6{\rm Tr}(Y_u Y_u^\dagger Y_u Y_u^\dagger),\end{aligned} \tag{B10}$$

$$\begin{aligned}\beta_{\lambda_{HS}}^{(1)} = {}& -\frac{9}{10}g_1^2\lambda_{HS} - \frac{9}{10}g_{YB}^2\lambda_{HS} - \frac{9}{2}g_2^2\lambda_{HS} - 81g_B^2\lambda_{HS}(\Theta_B^{\rm sum}) - 81g_{BY}^2\lambda_{HS}(\Theta_B^{\rm sum}) + 12\lambda_H\lambda_{HS} + 8\lambda_S\lambda_{HS} \\ & + 4\lambda_{HS}^2 + 2\lambda_{HS}|y_2|^2\Theta_\Psi + 2\lambda_{HS}|y_3|^2\Theta_\Psi + 2\lambda_{HS}|y_4|^2\Theta_\Psi + 4\lambda_{HS}|y_\Psi|^2\Theta_\Psi + 2\lambda_{HS}|y_\xi|^2\Theta_\xi \\ & + 2y_1^*(-2y_\Psi y_\xi y_2^* + y_1(-2|y_\Psi|^2 - 2|y_\xi|^2 + \lambda_{HS}))\Theta_\Psi - 4y_\chi y_\Psi y_3^* y_4^*(\Theta_\chi\Theta_\Psi) - 4y_\Psi|y_2|^2 y_\Psi^*\Theta_\Psi \\ & - 4y_\Psi|y_3|^2 y_\Psi^*\Theta_\Psi - 4y_\Psi|y_4|^2 y_\Psi^*\Theta_\Psi + 2y_\chi^*(-2y_3 y_4 y_\Psi^* - 2y_\chi|y_3|^2 - 2y_\chi|y_4|^2 + \lambda_{HS}y_\chi)\Theta_\chi \\ & - 4y_\xi|y_2|^2 y_\xi^*\Theta_\xi - 4y_1 y_2 y_\Psi^* y_\xi^*(\Theta_\Psi\Theta_\xi) + 6\lambda_{HS}{\rm Tr}(Y_d Y_d^\dagger) + 2\lambda_{HS}{\rm Tr}(Y_e Y_e^\dagger) + 6\lambda_{HS}{\rm Tr}(Y_u Y_u^\dagger),\end{aligned} \tag{B11}$$

$$\begin{aligned}\beta_{\lambda_S}^{(1)} = {}& \frac{2187}{2}g_B^4(\Theta_B^{\rm sum}) - 162g_B^2\lambda_S(\Theta_B^{\rm sum}) - 162g_{BY}^2\lambda_S(\Theta_B^{\rm sum}) + 20\lambda_S^2 + 2\lambda_{HS}^2 + 4\lambda_S|y_\chi|^2\Theta_\chi + 8\lambda_S|y_\Psi|^2\Theta_\Psi \\ & + 4\lambda_S|y_\xi|^2\Theta_\xi - 2|y_\chi|^4\Theta_\chi - 4|y_\Psi|^4\Theta_\Psi - 2|y_\xi|^4\Theta_\xi.\end{aligned} \tag{B12}$$

3. Yukawa couplings

For each Yukawa RGE the extra fermion dependent pieces are multiplied by the threshold(s) of the fermion(s) appearing in that term; the $U(1)_B$-gauge pieces are multiplied by the conservative $\Theta_B^{\rm sum}$ where indicated.

$$\beta_{Y_u}^{(1)} = -\frac{3}{2}(-Y_u Y_u^\dagger Y_u + Y_u Y_d^\dagger Y_d) + Y_u\Big(-\frac{17}{20}g_1^2 - \frac{17}{20}g_{YB}^2 - \frac{9}{4}g_2^2 - 8g_3^2 - \sqrt{\frac{5}{2}}g_{YB}g_B - g_B^2 - \sqrt{\frac{5}{2}}g_1 g_{BY} - g_{BY}^2 + |y_1|^2\Theta_\Psi + |y_2|^2\Theta_\Psi + |y_3|^2\Theta_\Psi + |y_4|^2\Theta_\Psi + 3\mathrm{Tr}(Y_d Y_d^\dagger) + \mathrm{Tr}(Y_e Y_e^\dagger) + 3\mathrm{Tr}(Y_u Y_u^\dagger)\Big), \tag{B13}$$

$$\beta_{Y_d}^{(1)} = \frac{3}{2}(-Y_d Y_u^\dagger Y_u + Y_d Y_d^\dagger Y_d) + Y_d\Big(-\frac{1}{4}g_1^2 - \frac{1}{4}g_{YB}^2 - \frac{9}{4}g_2^2 - 8g_3^2 + \frac{1}{\sqrt{10}}g_{YB}g_B - g_B^2 + \frac{1}{\sqrt{10}}g_1 g_{BY} - g_{BY}^2 + |y_1|^2\Theta_\Psi + |y_2|^2\Theta_\Psi + |y_3|^2\Theta_\Psi + |y_4|^2\Theta_\Psi + 3\mathrm{Tr}(Y_d Y_d^\dagger) + \mathrm{Tr}(Y_e Y_e^\dagger) + 3\mathrm{Tr}(Y_u Y_u^\dagger)\Big), \tag{B14}$$

$$\beta_{Y_e}^{(1)} = \frac{3}{2}Y_e Y_e^\dagger Y_e + Y_e\Big(3\mathrm{Tr}(Y_d Y_d^\dagger) + 3\mathrm{Tr}(Y_u Y_u^\dagger) - \frac{9}{4}g_1^2 - \frac{9}{4}g_2^2 - \frac{9}{4}g_{YB}^2 + |y_1|^2\Theta_\Psi + |y_2|^2\Theta_\Psi + |y_3|^2\Theta_\Psi + |y_4|^2\Theta_\Psi + \mathrm{Tr}(Y_e Y_e^\dagger)\Big). \tag{B15}$$

$$\beta_{y_4}^{(1)} = \frac{1}{20}y_4\Big(-9g_1^2 - 9g_{YB}^2 - 45g_2^2 - 36\sqrt{10}g_{YB}g_B(\Theta_B^{\rm sum}) - 720g_B^2(\Theta_B^{\rm sum}) - 36\sqrt{10}g_1 g_{BY}(\Theta_B^{\rm sum}) - 720g_{BY}^2(\Theta_B^{\rm sum}) + 10|y_\chi|^2\Theta_\chi + 20|y_1|^2\Theta_\Psi - 10|y_2|^2\Theta_\Psi + 20|y_3|^2\Theta_\Psi + 50|y_4|^2\Theta_\Psi + 10|y_\Psi|^2\Theta_\Psi + 60\mathrm{Tr}(Y_d Y_d^\dagger) + 20\mathrm{Tr}(Y_e Y_e^\dagger) + 60\mathrm{Tr}(Y_u Y_u^\dagger)\Big), \tag{B16}$$

$$\beta_{y_2}^{(1)} = \frac{1}{20}y_2\Big(-45g_1^2 - 45g_{YB}^2 - 45g_2^2 - 108\sqrt{10}g_{YB}g_B(\Theta_B^{\rm sum}) - 720g_B^2(\Theta_B^{\rm sum}) - 108\sqrt{10}g_1 g_{BY}(\Theta_B^{\rm sum}) - 720g_{BY}^2(\Theta_B^{\rm sum}) + 20|y_1|^2\Theta_\Psi + 50|y_2|^2\Theta_\Psi + 20|y_3|^2\Theta_\Psi - 10|y_4|^2\Theta_\Psi + 10|y_\Psi|^2\Theta_\Psi + 10|y_\xi|^2\Theta_\xi + 60\mathrm{Tr}(Y_d Y_d^\dagger) + 20\mathrm{Tr}(Y_e Y_e^\dagger) + 60\mathrm{Tr}(Y_u Y_u^\dagger)\Big), \tag{B17}$$

$$\beta_{y_\chi}^{(1)} = \frac{1}{2}y_\chi\big(2|y_3|^2\Theta_\Psi + 2|y_4|^2\Theta_\Psi + 2|y_\xi|^2\Theta_\xi - 45g_B^2(\Theta_B^{\rm sum}) - 45g_{BY}^2(\Theta_B^{\rm sum}) + 4|y_\chi|^2\Theta_\chi + 4|y_\Psi|^2\Theta_\Psi\big), \tag{B18}$$

$$\beta_{y_\xi}^{(1)} = \frac{1}{10}y_\xi\Big(-36g_1^2 - 36g_{YB}^2 - 18\sqrt{10}g_{YB}g_B(\Theta_B^{\rm sum}) - 225g_B^2(\Theta_B^{\rm sum}) - 18\sqrt{10}g_1 g_{BY}(\Theta_B^{\rm sum}) - 225g_{BY}^2(\Theta_B^{\rm sum}) + 10|y_\chi|^2\Theta_\chi + 10|y_1|^2\Theta_\Psi + 10|y_2|^2\Theta_\Psi + 20|y_\Psi|^2\Theta_\Psi + 20|y_\xi|^2\Theta_\xi\Big), \tag{B19}$$

$$\beta_{y_\Psi}^{(1)} = \frac{1}{10}y_\Psi\Big(-9g_1^2 - 9g_{YB}^2 - 45g_2^2 - 9\sqrt{10}g_{YB}g_B(\Theta_B^{\rm sum}) - 225g_B^2(\Theta_B^{\rm sum}) - 9\sqrt{10}g_1 g_{BY}(\Theta_B^{\rm sum}) - 225g_{BY}^2(\Theta_B^{\rm sum}) + 10|y_\chi|^2\Theta_\chi + 5|y_1|^2\Theta_\Psi + 5|y_2|^2\Theta_\Psi + 5|y_3|^2\Theta_\Psi + 5|y_4|^2\Theta_\Psi + 30|y_\Psi|^2\Theta_\Psi + 10|y_\xi|^2\Theta_\xi\Big), \tag{B20}$$

$$\beta_{y_3}^{(1)} = \frac{1}{20}y_3\Big(-9g_1^2 - 9g_{YB}^2 - 45g_2^2 + 18\sqrt{10}g_{YB}g_B(\Theta_B^{\rm sum}) - 180g_B^2(\Theta_B^{\rm sum}) + 18\sqrt{10}g_1 g_{BY}(\Theta_B^{\rm sum}) - 180g_{BY}^2(\Theta_B^{\rm sum}) + 10|y_\chi|^2\Theta_\chi - 10|y_1|^2\Theta_\Psi + 20|y_2|^2\Theta_\Psi + 50|y_3|^2\Theta_\Psi + 20|y_4|^2\Theta_\Psi + 10|y_\Psi|^2\Theta_\Psi + 60\mathrm{Tr}(Y_d Y_d^\dagger) + 20\mathrm{Tr}(Y_e Y_e^\dagger) + 60\mathrm{Tr}(Y_u Y_u^\dagger)\Big), \tag{B21}$$

$$\beta^{(1)}_{y_1} = \frac{1}{20} y_1 \Big(-45 g_1^2 - 45 g_{YB}^2 - 45 g_2^2 + 54\sqrt{10} g_{YB} g_B(\Theta_B^{\rm sum}) - 180 g_B^2(\Theta_B^{\rm sum}) + 54\sqrt{10} g_1 g_{BY}(\Theta_B^{\rm sum}) - 180 g_{BY}^2(\Theta_B^{\rm sum}) + 50|y_1|^2\Theta_\Psi + 20|y_2|^2\Theta_\Psi - 10|y_3|^2\Theta_\Psi + 20|y_4|^2\Theta_\Psi + 10|y_\Psi|^2\Theta_\Psi + 10|y_\xi|^2\Theta_\xi + 60{\rm Tr}(Y_d Y_d^\dagger) + 20{\rm Tr}(Y_e Y_e^\dagger) + 60{\rm Tr}(Y_u Y_u^\dagger) \Big). \tag{B22}$$

4. Mass terms

$$\beta^{(1)}_{\mu_H^2} = 2\lambda_{HS}\mu_S^2\Theta_S - \frac{9}{10} g_1^2 \mu_H^2 - \frac{9}{10} g_{YB}^2 \mu_H^2 - \frac{9}{2} g_2^2 \mu_H^2 + 12\lambda_H \mu_H^2 + 2\mu_H^2|y_1|^2\Theta_\Psi + 2\mu_H^2|y_2|^2\Theta_\Psi + 2\mu_H^2|y_3|^2\Theta_\Psi + 2\mu_H^2|y_4|^2\Theta_\Psi + 6\mu_H^2{\rm Tr}(Y_d Y_d^\dagger) + 2\mu_H^2{\rm Tr}(Y_e Y_e^\dagger) + 6\mu_H^2{\rm Tr}(Y_u Y_u^\dagger), \tag{B23}$$

$$\beta^{(1)}_{\mu_S^2} = 2\mu_S^2|y_\chi|^2\Theta_\chi + 2\mu_S^2|y_\xi|^2\Theta_\xi + 4\lambda_{HS}\mu_H^2 + 4\mu_S^2|y_\Psi|^2\Theta_\Psi - 81 g_{BY}^2\mu_S^2(\Theta_B^{\rm sum}) - 81 g_B^2\mu_S^2(\Theta_B^{\rm sum}) + 8\lambda_S\mu_S^2. \tag{B24}$$

5. Running of the couplings

For the numerical evaluation of the renormalization group, we adopt a simplified form of all the beta functions. In this approach, all SM couplings are neglected except for the gauge couplings, the top-quark Yukawa coupling, and the Higgs quartic coupling. In Fig. 9, we show the running of the couplings from electroweak scale upto Planck scale for representative parameter values $\lambda_S = 10^{-3}$, $\theta_{\rm DM} = 0.001$, $v_B = 10^5$ GeV, $y_\chi = 0.01$, $y_\psi = 0.05$, $y_\xi = 0.1$ while varying the portal coupling λ_{HS}. All other dimensionless couplings other than those shown in the figure remain almost constant upto Planck scale. In Fig. 9, the plot on the left shows the minimum value of $\lambda_{HS} \sim 0.008$ for which λ_H remains positive throughout, which means that the Higgs potential is stable. The plot on the right demonstrate the maximum value of $\lambda_{HS} = 0.021$ allowed beyond which the perturbativity limit of the model is broken since λ_H hits the Laundau pole. This allowed range of λ_{HS} changes depending on values of λ_S and $\theta_{\rm DM}$. From a phenomenological perspective, we are interested in λ_S and $\theta_{\rm DM}$ values close to 10^{-3} and 0.001 respectively, hence for the analysis of this paper we choose $\lambda_{HS} = 0.01$.

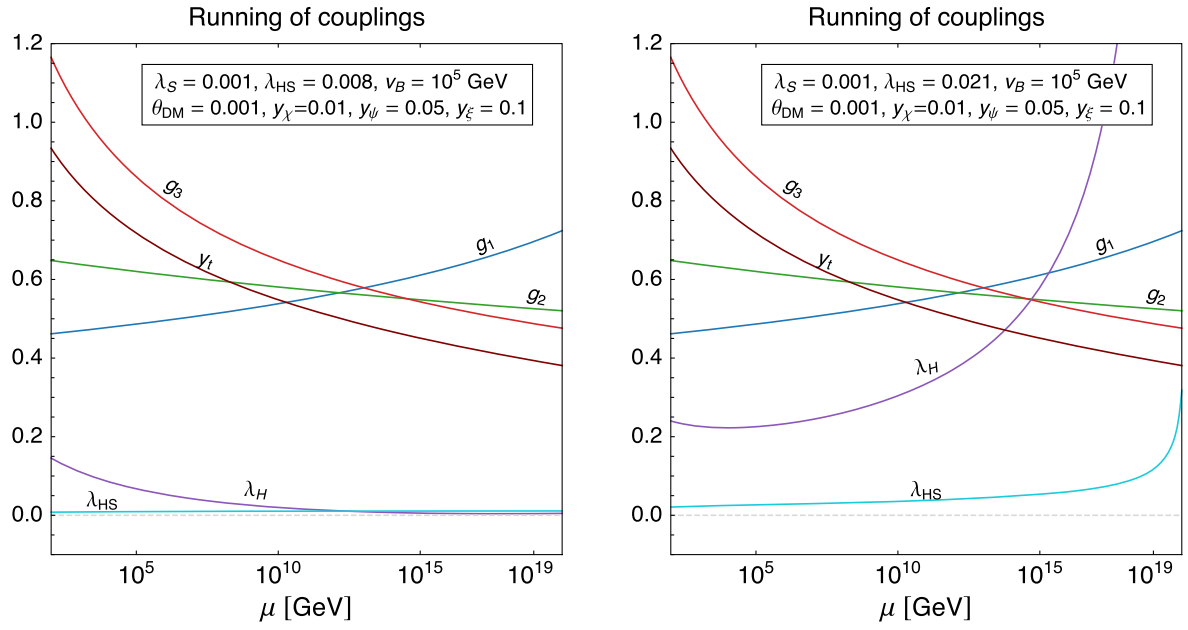


FIG. 9. Running of the coupling constants in our model for representative parameter values. The left plot shows the minimum λ_{HS} allowed such that the Higgs potential remains stable upto Planck scale, meaning λ_H remains positive. The plot on the right shows the maximum value of λ_{HS} such that λ_H does not hit the Laundau pole breaking the perturbativity of the model.

For the random parameter scan (see Fig. 7), we impose the stability of the Higgs potential and perturbativity conditions from RGEs as described in the main text.

We highlight that imposing vacuum stability and perturbativity up to the Planck scale is a conservative requirement to ensure UV robustness. This assumption is not strictly necessary, and the effective theory may remain valid only up to a lower cutoff scale set by the heaviest states in the spectrum, which in our model is around the $U(1)_B$ breaking scale v_B. Relaxing this requirement would enlarge the allowed parameter space, e.g., a larger value of λ_{HS}, however, without qualitatively affecting our conclusions regarding the phase transition dynamics and the resulting gravitational wave signals.

[1] A. Einstein, Ann. Phys. (Berlin) **49**, 769 (1916).
[2] N. Aghanim *et al.* (Planck Collaboration), Astron. Astrophys. **641**, A6 (2020); **652**, C4(E) (2021.
[3] Y. Fukuda *et al.* (Super-Kamiokande Collaboration), Phys. Rev. Lett. **81**, 1562 (1998).
[4] Q. R. Ahmad *et al.* (SNO Collaboration), Phys. Rev. Lett. **89**, 011301 (2002).
[5] M. H. Ahn *et al.* (K2K Collaboration), Phys. Rev. Lett. **90**, 041801 (2003).
[6] W. H. Julian, Astrophys. J. **148**, 175 (1967).
[7] M. Tegmark *et al.* (SDSS Collaboration), Phys. Rev. D **69**, 103501 (2004).
[8] J. C. Pati and A. Salam, Phys. Rev. D **8**, 1240 (1973).
[9] J. C. Pati and A. Salam, Phys. Rev. D **10**, 275 (1974); **11**, 703(E) (1975).
[10] R. N. Mohapatra and J. C. Pati, Phys. Rev. D **11**, 2558 (1975).
[11] R. N. Mohapatra and J. C. Pati, Phys. Rev. D **11**, 566 (1975).
[12] H. Georgi and S. L. Glashow, Phys. Rev. Lett. **32**, 438 (1974).
[13] H. Georgi, H. R. Quinn, and S. Weinberg, Phys. Rev. Lett. **33**, 451 (1974).
[14] H. Georgi, AIP Conf. Proc. **23**, 575 (1975).
[15] A. De Rujula, H. Georgi, and S. L. Glashow, Phys. Rev. D **12**, 147 (1975).
[16] H. Fritzsch and P. Minkowski, Ann. Phys. (N.Y.) **93**, 193 (1975).
[17] A. Pais, Phys. Rev. D **8**, 1844 (1973).
[18] M. Duerr, P. Fileviez Perez, and M. B. Wise, Phys. Rev. Lett. **110**, 231801 (2013).
[19] U. Patel and S. Patra, arXiv:2204.11551.
[20] P. Fileviez Perez and M. Wise, Phys. Rev. D **82**, 011901 (2010); **82**, 079901(E) (2010).
[21] P. Fileviez Perez and M. B. Wise, J. High Energy Phys. 08 (2011) 068.
[22] T. R. Dulaney, P. Fileviez Perez, and M. B. Wise, Phys. Rev. D **83**, 023520 (2011).
[23] B. P. Abbott *et al.* (LIGO Scientific and Virgo Collaborations), Phys. Rev. Lett. **116**, 061102 (2016).
[24] G. Agazie *et al.* (NANOGrav Collaboration), Astrophys. J. Lett. **951**, L8 (2023).
[25] A. Afzal *et al.* (NANOGrav Collaboration), Astrophys. J. Lett. **951**, L11 (2023); **971**, L27(E) (2024).
[26] M. Hindmarsh, Phys. Rev. Lett. **120**, 071301 (2018).
[27] Z. Arzoumanian *et al.* (NANOGRAV Collaboration), Astrophys. J. **859**, 47 (2018).
[28] K. Aggarwal *et al.*, Astrophys. J. **880**, 2 (2019).
[29] A. Brazier *et al.*, arXiv:1908.05356.
[30] Z. Arzoumanian *et al.* (NANOGrav Collaboration), Astrophys. J. Lett. **905**, L34 (2020).
[31] C. Caprini, R. Jinno, T. Konstandin, A. Roper Pol, H. Rubira, and I. Stomberg, J. High Energy Phys. 07 (2025) 217.
[32] C. Caprini, R. Jinno, M. Lewicki, E. Madge, M. Merchand, G. Nardini, M. Pieroni, A. Roper Pol, and V. Vaskonen (LISA Cosmology Working Group), J. Cosmol. Astropart. Phys. 10 (2024) 020.
[33] C. Caprini, R. Durrer, and G. Servant, J. Cosmol. Astropart. Phys. 12 (2009) 024.
[34] M. Hindmarsh, S. J. Huber, K. Rummukainen, and D. J. Weir, Phys. Rev. Lett. **112**, 041301 (2014).
[35] S. J. Huber and T. Konstandin, J. Cosmol. Astropart. Phys. 09 (2008) 022.
[36] G. W. Anderson and L. J. Hall, Phys. Rev. D **45**, 2685 (1992).
[37] P. Schwaller, Phys. Rev. Lett. **115**, 181101 (2015).
[38] M. Breitbach *et al.*, J. High Energy Phys. 07 (2019) 044.
[39] K. Hashino, M. Kakizaki, S. Kanemura, P. Ko, and T. Matsui, Phys. Rev. D **98**, 015053 (2018).
[40] D. Borah, A. Dasgupta, and S. K. Kang, Phys. Rev. D **104**, 063501 (2021).
[41] A. Dasgupta, P. S. B. Dev, T. Han, R. Padhan, S. Wang, and K. Xie, J. High Energy Phys. 12 (2023) 011.
[42] V. Brdar, M. Finetti, M. Matteini, A. P. Morais, and M. Nemevšek, Comput. Phys. Commun. **323**, 110119 (2026).
[43] V. Brdar, A. J. Helmboldt, and J. Kubo, J. Cosmol. Astropart. Phys. 02 (2019) 021.
[44] L. Gráf, S. Jana, A. Kaladharan, and S. Saad, J. Cosmol. Astropart. Phys. 05 (2022) 003.
[45] S. Karmakar and D. Ringe, Phys. Rev. D **109**, 075034 (2024).
[46] T. Alanne, N. Benincasa, M. Heikinheimo, K. Kannike, V. Keus, N. Koivunen, and K. Tuominen, J. High Energy Phys. 10 (2020) 080.
[47] Z. Chen, K. Ye, and M. Zhang, Phys. Rev. D **107**, 095027 (2023).
[48] T. Abe and K. Hashino, Phys. Rev. D **108**, 015033 (2023).
[49] T. Srivastava, J. Das, A. Ghosh, and A. Chaudhuri, J. Cosmol. Astropart. Phys. 02 (2026) 032.

[50] T. Bringmann, T. E. Gonzalo, F. Kahlhoefer, J. Matuszak, and C. Tasillo, J. Cosmol. Astropart. Phys. 05 (2024) 065.
[51] M. Hosseini, S. Yaser Ayazi, and A. Mohamadnejad, Eur. Phys. J. C **84**, 485 (2024).
[52] D. Borah, A. Dasgupta, and S. K. Kang, J. Cosmol. Astropart. Phys. 12 (2021) 039.
[53] V. V. Khoze and D. L. Milne, Phys. Rev. D **107**, 095012 (2023).
[54] P. Ghosh, T. Ghosh, and S. Roy, J. High Energy Phys. 10 (2023) 057.
[55] S. Roy, Phys. Rev. D **111**, 015037 (2025).
[56] D. Hooper, G. Krnjaic, D. Rocha, and S. Roy, arXiv:2507.22975.
[57] A. Chatterjee, A. Datta, and S. Roy, J. High Energy Phys. 06 (2022) 108.
[58] P. Borah, P. Ghosh, and A. K. Saha, J. Cosmol. Astropart. Phys. 05 (2025) 035.
[59] T. Abe, K. S. Babu, and A. Kaladharan, J. Cosmol. Astropart. Phys. 07 (2024) 048.
[60] C. F. P. da Silva (LUX Collaboration), in *Proceedings of the 52nd Rencontres de Moriond on Very High Energy Phenomena in the Universe* (2017), pp. 199–209, arXiv:1710.03572.
[61] E. Aprile *et al.* (XENON100 Collaboration), Phys. Rev. Lett. **109**, 181301 (2012).
[62] A. Tan *et al.* (PandaX-II Collaboration), Phys. Rev. Lett. **117**, 121303 (2016).
[63] X. Cui *et al.* (PandaX-II Collaboration), Phys. Rev. Lett. **119**, 181302 (2017).
[64] E. Aprile *et al.* (XENON Collaboration), J. Cosmol. Astropart. Phys. 04 (2016) 027.
[65] E. Aprile *et al.* (XENON Collaboration), Phys. Rev. Lett. **121**, 111302 (2018).
[66] O. Adriani *et al.* (PAMELA Collaboration), Phys. Rev. Lett. **111**, 081102 (2013).
[67] O. Adriani *et al.* (PAMELA Collaboration), Phys. Rev. Lett. **106**, 201101 (2011).
[68] C. Corti (AMS Collaboration), in *Proceedings of the 10th International Symposium on Cosmology and Particle Astrophysics* (2014), arXiv:1402.0437.
[69] W. B. Atwood *et al.* (Fermi-LAT Collaboration), Astrophys. J. **697**, 1071 (2009).
[70] M. G. Aartsen *et al.* (IceCube Collaboration), Eur. Phys. J. C **77**, 627 (2017).
[71] M. G. Aartsen *et al.* (IceCube Collaboration), Eur. Phys. J. C **78**, 831 (2018).
[72] S. Bhattacharya, P. Ghosh, N. Sahoo, and N. Sahu, Front. Phys. **7**, 80 (2019).
[73] S. Bhattacharya, N. Sahoo, and N. Sahu, Phys. Rev. D **96**, 035010 (2017).
[74] K. Ghorbani, J. Cosmol. Astropart. Phys. 01 (2015) 015.
[75] M. Dutta, S. Bhattacharya, P. Ghosh, and N. Sahu, Springer Proc. Phys. **277**, 685 (2022).
[76] B. Barman, A. Dutta Banik, and A. Paul, Phys. Rev. D **101**, 055028 (2020).
[77] P. Konar, A. Mukherjee, A. K. Saha, and S. Show, Phys. Rev. D **102**, 015024 (2020).
[78] P. Konar, A. Mukherjee, A. K. Saha, and S. Show, J. High Energy Phys. 03 (2021) 044.
[79] M. Sarazin, J. Bernigaud, and B. Herrmann, J. High Energy Phys. 12 (2021) 116.
[80] P. Ghosh, S. Mahapatra, N. Narendra, and N. Sahu, Phys. Rev. D **106**, 015001 (2022).
[81] D. Borah, M. Dutta, S. Mahapatra, and N. Sahu, Phys. Rev. D **105**, 075019 (2022).
[82] S. Mishra, N. Narendra, P. K. Panda, and N. Sahoo, Nucl. Phys. **B981**, 115855 (2022).
[83] D. Borah, S. Mahapatra, and N. Sahu, Phys. Lett. B **831**, 137196 (2022).
[84] P. K. Paul, S. K. Sahoo, and N. Sahu, J. Cosmol. Astropart. Phys. 10 (2025) 053.
[85] D. Borah, S. Mahapatra, D. Nanda, S. K. Sahoo, and N. Sahu, J. High Energy Phys. 05 (2024) 096.
[86] P. Borah and P. Ghosh, arXiv:2505.16521.
[87] D. N. Spergel *et al.* (WMAP Collaboration), Astrophys. J. Suppl. Ser. **148**, 175 (2003).
[88] Taramati, R. Sahu, U. Patel, K. Ghosh, and S. Patra, J. High Energy Phys. 01 (2025) 159.
[89] P. Fileviez Pérez, E. Golias, R.-H. Li, and C. Murgui, Phys. Rev. D **99**, 035009 (2019).
[90] C. D. Carone and H. Murayama, Phys. Rev. D **52**, 484 (1995).
[91] P. Fileviez Perez, S. Ohmer, and H. H. Patel, Phys. Lett. B **735**, 283 (2014).
[92] E. Ma, Phys. Lett. B **813**, 136066 (2021).
[93] P. Fileviez Perez and C. Murgui, Phys. Rev. D **100**, 035041 (2019).
[94] C. Murgui and P. Fileviez Perez, J. High Energy Phys. 01 (2020) 064.
[95] M. Duerr and P. Fileviez Perez, Phys. Rev. D **91**, 095001 (2015).
[96] S. El Hedri and K. Nordström, SciPost Phys. **6**, 020 (2019).
[97] M. Duerr and P. Fileviez Perez, Phys. Lett. B **732**, 101 (2014).
[98] J. Ellis, M. Fairbairn, and P. Tunney, arXiv:1807.02503.
[99] J. Baker *et al.*, arXiv:1907.06482.
[100] N. Seto, S. Kawamura, and T. Nakamura, Phys. Rev. Lett. **87**, 221103 (2001).
[101] K. Yagi and N. Seto, Phys. Rev. D **83**, 044011 (2011); **95**, 109901(E) (2017).
[102] J. Crowder and N. J. Cornish, Phys. Rev. D **72**, 083005 (2005).
[103] V. Corbin and N. J. Cornish, Classical Quantum Gravity **23**, 2435 (2006).
[104] M. Punturo *et al.*, Classical Quantum Gravity **27**, 194002 (2010).
[105] S. Hild *et al.*, Classical Quantum Gravity **28**, 094013 (2011).
[106] G. M. Pruna and T. Robens, Phys. Rev. D **88**, 115012 (2013).
[107] S. Patra, W. Rodejohann, and C. E. Yaguna, J. High Energy Phys. 09 (2016) 076.
[108] F. Halzen and A. D. Martin, *Quarks and Leptons: An Introductory Course in Modern Particle Physics* (John Wiley & Sons, Chichester, United Kingdom, 1984).
[109] M. Li, Q.-S. Yan, Y. Zhang, and Z. Zhao, J. High Energy Phys. 03 (2021) 267.
[110] S. R. Coleman and E. J. Weinberg, Phys. Rev. D **7**, 1888 (1973).

[111] P. Basler, M. Krause, M. Muhlleitner, J. Wittbrodt, and A. Wlotzka, J. High Energy Phys. 02 (2017) 121.
[112] M. Quiros, in ICTP Summer School in High-Energy Physics and Cosmology, arXiv:hep-ph/9901312.
[113] L. Dolan and R. Jackiw, Phys. Rev. D **9**, 3320 (1974).
[114] P. Bittar, S. Roy, and C. E. M. Wagner, J. High Energy Phys. 12 (2025) 021.
[115] R. R. Parwani, Phys. Rev. D **45**, 4695 (1992); **48**, 5965(E) (1993).
[116] P. B. Arnold and O. Espinosa, Phys. Rev. D **47**, 3546 (1993); **50**, 6662(E) (1994).
[117] M. Carena, G. Nardini, M. Quiros, and C. E. M. Wagner, Nucl. Phys. **B812**, 243 (2009).
[118] P. Athron, C. Balázs, A. Fowlie, L. Morris, and L. Wu, Prog. Part. Nucl. Phys. **135**, 104094 (2024).
[119] M. E. Carrington, Phys. Rev. D **45**, 2933 (1992).
[120] A. D. Linde, Phys. Lett. **100B**, 37 (1981).
[121] S. R. Coleman, Phys. Rev. D **15**, 2929 (1977); **16**, 1248(E) (1977).
[122] Z. A. Borboruah and U. A. Yajnik, Phys. Rev. D **110**, 043016 (2024).
[123] A. H. Guth and E. J. Weinberg, Phys. Rev. D **23**, 876 (1981).
[124] V. K. S. Shante and S. Kirkpatrick, Adv. Phys. **20**, 325 (1971).
[125] J. R. Espinosa, T. Konstandin, J. M. No, and G. Servant, J. Cosmol. Astropart. Phys. 06 (2010) 028.
[126] M. Kamionkowski, A. Kosowsky, and M. S. Turner, Phys. Rev. D **49**, 2837 (1994).
[127] R. Jackiw, Phys. Rev. D **9**, 1686 (1974).
[128] R. Fukuda and T. Kugo, Phys. Rev. D **13**, 3469 (1976).
[129] N. K. Nielsen, Nucl. Phys. **B101**, 173 (1975).
[130] H. H. Patel and M. J. Ramsey-Musolf, J. High Energy Phys. 07 (2011) 029.
[131] M. Garny and T. Konstandin, J. High Energy Phys. 07 (2012) 189.
[132] C. Wainwright, S. Profumo, and M. J. Ramsey-Musolf, Phys. Rev. D **84**, 023521 (2011).
[133] C. L. Wainwright, S. Profumo, and M. J. Ramsey-Musolf, Phys. Rev. D **86**, 083537 (2012).
[134] A. Andreassen, W. Frost, and M. D. Schwartz, Phys. Rev. D **91**, 016009 (2015).
[135] A. Andreassen, W. Frost, and M. D. Schwartz, Phys. Rev. Lett. **113**, 241801 (2014).
[136] J. R. Espinosa, M. Garny, T. Konstandin, and A. Riotto, Phys. Rev. D **95**, 056004 (2017).
[137] A. Kosowsky, M. S. Turner, and R. Watkins, Phys. Rev. D **45**, 4514 (1992).
[138] C. Caprini and R. Durrer, Phys. Rev. D **74**, 063521 (2006).
[139] C. Caprini *et al.*, J. Cosmol. Astropart. Phys. 04 (2016) 001.
[140] A. Kosowsky and M. S. Turner, Phys. Rev. D **47**, 4372 (1993).
[141] C. Caprini and D. G. Figueroa, Classical Quantum Gravity **35**, 163001 (2018).
[142] S. J. Huber and T. Konstandin, J. Cosmol. Astropart. Phys. 09 (2008) 022.
[143] D. J. Weir, Phys. Rev. D **93**, 124037 (2016).
[144] M. Kamionkowski, A. Kosowsky, and M. S. Turner, Phys. Rev. D **49**, 2837 (1994).
[145] M. Hindmarsh, S. J. Huber, K. Rummukainen, and D. J. Weir, Phys. Rev. D **92**, 123009 (2015).
[146] H.-K. Guo, K. Sinha, D. Vagie, and G. White, J. Cosmol. Astropart. Phys. 01 (2021) 001.
[147] M. Lewicki, M. Merchand, and M. Zych, J. High Energy Phys. 02 (2022) 017.
[148] K. Schmitz, J. High Energy Phys. 01 (2021) 097.
[149] C. Caprini, M. Hindmarsh, S. Huber, T. Konstandin, J. Kozaczuk, G. Nardini, J. M. No, A. Petiteau, P. Schwaller, G. Servant, and D. J. Weir, J. Cosmol. Astropart. Phys. 04 (2016) 001.
[150] M. Hindmarsh, S. J. Huber, K. Rummukainen, and D. J. Weir, Phys. Rev. D **96**, 103520 (2017); **101**, 089902(E) (2020).
[151] C. Caprini, R. Durrer, and G. Servant, J. Cosmol. Astropart. Phys. 12 (2009) 024.
[152] P. Binétruy, A. Bohé, C. Caprini, and J.-F. Dufaux, J. Cosmol. Astropart. Phys. 06 (2012) 027.
[153] P. Amaro-Seoane *et al.* (LISA Collaboration), arXiv:1702.00786.
[154] B. P. Abbott *et al.* (LIGO Scientific Collaboration), Classical Quantum Gravity **34**, 044001 (2017).
[155] D. Reitze *et al.*, Bull. Am. Astron. Soc. **51**, 035 (2019).
[156] R. H. Cyburt, B. D. Fields, K. A. Olive, and T.-H. Yeh, Rev. Mod. Phys. **88**, 015004 (2016).
[157] S. Aiola *et al.* (CMB-HD Collaboration), arXiv:2203.05728.
[158] D. Adak, A. Sen, S. Basak, J. Delabrouille, T. Ghosh, A. Rotti, G. Martínez-Solaeche, and T. Souradeep, Mon. Not. R. Astron. Soc. **514**, 3002 (2022).
[159] K. N. Abazajian and M. Kaplinghat, Annu. Rev. Nucl. Part. Sci. **66**, 401 (2016).
[160] M. Alvarez *et al.*, Bull. Am. Astron. Soc. **51**, 194 (2019).
[161] A. Vilenkin and E. P. S. Shellard, *Cosmic Strings and Other Topological Defects* (Cambridge University Press, Cambridge, England, 2000).
[162] H. B. Nielsen and P. Olesen, Nucl. Phys. **B61**, 45 (1973).
[163] T. W. B. Kibble, J. Phys. A **9**, 1387 (1976).
[164] T. Vachaspati and A. Vilenkin, Phys. Rev. D **31**, 3052 (1985).
[165] Y. Gouttenoire, G. Servant, and P. Simakachorn, J. Cosmol. Astropart. Phys. 07 (2020) 032.
[166] B. Allen and E. P. S. Shellard, Phys. Rev. D **45**, 1898 (1992).
[167] P. Auclair *et al.*, J. Cosmol. Astropart. Phys. 04 (2020) 034.
[168] J. J. Blanco-Pillado, K. D. Olum, and J. M. Wachter, Phys. Rev. D **100**, 123526 (2019).
[169] A. Ghoshal, A. Spalding, and G. White, arXiv:2512.14684.
[170] M. E. Peskin and T. Takeuchi, Phys. Rev. Lett. **65**, 964 (1990).
[171] M. E. Peskin and T. Takeuchi, Phys. Rev. D **46**, 381 (1992).
[172] D. C. Kennedy and P. Langacker, Phys. Rev. Lett. **65**, 2967 (1990); **66**, 395(E) (1991).
[173] T. Han, D. Marfatia, and R.-J. Zhang, Phys. Rev. D **62**, 125018 (2000).
[174] S. Navas *et al.* (Particle Data Group), Phys. Rev. D **110**, 030001 (2024).
[175] W. Porod, Comput. Phys. Commun. **153**, 275 (2003).

[176] P. Fileviez Perez, C. Murgui, and S. Ohmer, Phys. Rev. D **94**, 051701 (2016).
[177] G. Alguero, G. Belanger, F. Boudjema, S. Chakraborti, A. Goudelis, S. Kraml, A. Mjallal, and A. Pukhov, Comput. Phys. Commun. **299**, 109133 (2024).
[178] A. Abdukerim *et al.* (PANDA-X and PandaX Collaborations), Sci. China Phys. Mech. Astron. **68**, 221011 (2025).
[179] J. Aalbers *et al.* (LZ Collaboration), Phys. Rev. Lett. **135**, 011802 (2025).
[180] E. Aprile *et al.* (XENON Collaboration), Phys. Rev. Lett. **135**, 221003 (2025).
[181] J. Conrad, arXiv:1411.1925.
[182] Z. A. Borboruah, D. Borah, L. Malhotra, and U. Patel, Phys. Rev. D **112**, 015022 (2025).
[183] M. Ackermann *et al.* (Fermi-LAT Collaboration), Phys. Rev. D **91**, 122002 (2015).
[184] F. Acero *et al.* (Fermi-LAT Collaboration), Astrophys. J. Suppl. Ser. **218**, 23 (2015).
[185] J. W. Foster, Y. Park, B. R. Safdi, Y. Soreq, and W. L. Xu, Phys. Rev. D **107**, 103047 (2023).
[186] M. Ackermann *et al.* (Fermi-LAT Collaboration), Phys. Rev. Lett. **107**, 241302 (2011).
[187] H. Abdallah *et al.* (H. E. S. S. Collaboration), Phys. Rev. Lett. **117**, 111301 (2016).
[188] H. Abdallah *et al.* (HESS Collaboration), Phys. Rev. Lett. **120**, 201101 (2018).
[189] B. S. Acharya *et al.* (CTA Consortium Collaboration), *Science with the Cherenkov Telescope Array* (World Scientific Publishing, Singapore, 2018).
[190] S. Abe *et al.* (CTAO Collaboration), J. Cosmol. Astropart. Phys. 07 (2024) 047.
[191] M. Aaboud *et al.* (ATLAS Collaboration), Phys. Rev. Lett. **121**, 081801 (2018).
[192] G. Aad *et al.* (ATLAS Collaboration), J. High Energy Phys. 11 (2020) 005; 04 (2021) 142(E).
[193] G. Aad *et al.* (ATLAS Collaboration), Phys. Rev. D **101**, 052005 (2020).
[194] A. M. Sirunyan *et al.* (CMS Collaboration), Phys. Lett. B **769**, 520 (2017).
[195] A. Djouadi, Phys. Rep. **457**, 1 (2008).
[196] M. Spira, A. Djouadi, D. Graudenz, and P. M. Zerwas, Nucl. Phys. **B453**, 17 (1995).
[197] M. Spira, Prog. Part. Nucl. Phys. **95**, 98 (2017).
[198] J. F. Gunion, H. E. Haber, G. L. Kane, and S. Dawson, *The Higgs Hunter's Guide* (Elsevier Science B.V., Amsterdam, 2000), Vol. 80.
[199] D. de Florian *et al.* (LHC Higgs Cross Section Working Group), CERN Yellow Rep. Monogr. **2**, 1 (2017).
[200] B. A. Dobrescu and F. Yu, Phys. Rev. D **109**, 035004 (2024).
[201] F. Yu, arXiv:1308.1077.
[202] A. Ekstedt, R. Enberg, G. Ingelman, J. Löfgren, and T. Mandal, J. High Energy Phys. 02 (2018) 152.
[203] CMS Collaboration, Searches for light higgsino-like charginos and neutralinos at the HL-LHC with the Phase-2 CMS detector, Technical Report No. CMS-PAS-FTR-18-001, CERN, Geneva, 2018.
[204] C. Helsens and M. Selvaggi, Search for high-mass resonances at FCC-hh, Technical Report No. CERN-ACC-2019-0028, CERN, Geneva, 2018, https://cds.cern.ch/record/2642473.
[205] C. M. Berggren (ILD Concept Group), Proc. Sci., EPS-HEP2021 (**2022**) 713 [arXiv:2111.02386].
[206] D. Curtin *et al.*, Rep. Prog. Phys. **82**, 116201 (2019).
[207] D. Curtin and J. S. Grewal, Phys. Rev. D **109**, 075017 (2024).
[208] A. Ariga *et al.* (FASER Collaboration), arXiv:1812.09139.
[209] A. Ariga *et al.* (FASER Collaboration), arXiv:1901.04468.
[210] H. Abreu *et al.* (FASER Collaboration), Eur. Phys. J. C **80**, 61 (2020).
[211] T. B. de Melo, S. Kovalenko, F. S. Queiroz, C. Siqueira, and Y. S. Villamizar, Phys. Rev. D **103**, 115001 (2021).
[212] P. S. B. Dev, W. Rodejohann, X.-J. Xu, and Y. Zhang, J. High Energy Phys. 06 (2021) 039.
[213] Z. S. Demiroglu (MOLLER Collaboration), Proc. Sci., SPIN2023 (**2024**) 141.
[214] T. Kitahara, T. Okui, G. Perez, Y. Soreq, and K. Tobioka, Phys. Rev. Lett. **124**, 071801 (2020).
[215] F. Ertas, F. Kahlhoefer, and C. Tasillo, J. Cosmol. Astropart. Phys. 02 (2022) 014.
[216] C. L. Wainwright, Comput. Phys. Commun. **183**, 2006 (2012).
[217] F. Staub, arXiv:0806.0538.
[218] W. Porod and F. Staub, Comput. Phys. Commun. **183**, 2458 (2012).
[219] K. Griest and D. Seckel, Phys. Rev. D **43**, 3191 (1991).
[220] M. Duerr, F. Kahlhoefer, K. Schmidt-Hoberg, T. Schwetz, and S. Vogl, J. High Energy Phys. 09 (2016) 042.